Ocean Modelling 181 (2023) 102154

Contents lists available at ScienceDirect

Ocean Modelling

journal homepage: www.elsevier.com/locate/ocemod

Remote internal wave forcing of regional ocean simulations near the U.S. West Coast

Oladeji Q. Siyanbola [a,*], Maarten C. Buijsman [a], Audrey Delpech [b], Lionel Renault [c], Roy Barkan [b,d], Jay F. Shriver [e], Brian K. Arbic [f], James C. McWilliams [b]

[a] School of Ocean Science and Engineering, University of Southern Mississippi, Stennis Space Center, MS, USA
[b] Department of Atmospheric and Ocean Sciences, UCLA, Los Angeles, CA, USA
[c] LEGOS, University of Toulouse, IRD, CNRS, CNES, UPS, Toulouse, France
[d] Porter School of the Environment and Earth Sciences, Tel Aviv University, Ramat Aviv, Israel
[e] Ocean Dynamics and Prediction Branch, Naval Research Laboratory, Stennis Space Center, MS, USA
[f] Department of Earth and Environmental Sciences, University of Michigan, Ann Arbor, MI, USA

ARTICLE INFO

Keywords:
Regional ocean modeling
High-frequency boundary forcing
Internal waves
Open boundary sensitivity
Model-data comparison
U.S. West Coast

ABSTRACT

Low mode internal waves are able to propagate across ocean basins and modulate ocean dynamics thousands of kilometers away from their generation sites. In this study, the impact of remotely generated internal waves on the internal wave energetics near the U.S. West Coast is investigated with realistically forced regional ocean simulations. At the open boundaries, we impose high-frequency oceanic state variables obtained from a global ocean simulation with realistic atmospheric and astronomical tidal forcing. We use the Discrete Fourier Transform (DFT) technique in separating ingoing and outgoing internal tide energy fluxes at the open boundaries in order to quantify internal tide reflections. Although internal tide reflections are reduced with increasing sponge viscosity and/or sponge layer width, reflection coefficients (λ) can be as high as 73%. In the presence of remote internal waves, the model variance and spatial correlations become more in agreement with both mooring and altimetry datasets. The results confirm that an improved internal wave continuum can be achieved in regional models with remote internal wave forcing at the open boundaries. However, care should be taken to avoid excessive reflections of internal waves from the interior at these boundaries.

1. Introduction

Internal waves are well known to extend their footprints into oceanographic measurements — in situ (e.g., Waterhouse et al., 2014), remotely sensed (e.g., Ray and Zaron, 2011, 2016), and acoustic measurements (e.g., Dushaw et al., 1995; Li et al., 2009). These baroclinic motions play a key role in multiple oceanic processes, including diapycnal mixing (e.g., Kunze et al., 2002), transport of sediments (e.g., Sinnett et al., 2018), and transport of high nutrient waters from the deep part of the ocean to the surface (e.g., Tuerena et al., 2019). The dissipation of barotropic tides by means of scattering into internal tides at rough bathymetry in the open ocean has been suggested to be responsible for half of the power required to maintain the meridional overturning circulation (Munk and Wunsch, 1998; Egbert and Ray, 2000, 2003). This demonstrates how important it is to track internal wave energy pathways from generation to dissipation to better understand the large-scale ocean circulation and ocean climate.

Although there is a growing effort directed towards increasing the resolution of oceanographic measurements, one of which is the upcoming Surface Water and Ocean Topography (SWOT) altimeter mission (Fu et al., 2012; Wang et al., 2018), the large spatio-temporal resolution of numerical ocean models cannot be matched. However, the ability of numerical ocean circulation models to resolve physical processes at smaller spatio-temporal scales such as sub-mesoscale eddies and internal waves, requires relatively fine horizontal and/or vertical grid resolutions (van Haren et al., 2004). Implementation of these resolutions in global ocean circulation models may incur a significant computational expense. To overcome this problem, regional ocean circulation models with resolutions much higher than are feasible in global simulations are used (e.g., Buijsman et al., 2012; Kelly et al., 2012; Kumar et al., 2019; Nelson et al., 2020).

Regional models are forced at the lateral open boundaries with data from climatologies and global or basin scale model simulations (e.g., Chassignet et al., 2007; Zamudio et al., 2008; Buijsman et al., 2012; Chen et al., 2013) to prevent significant drift away from the realistic ocean state. Choosing the right open boundary conditions

* Corresponding author.
E-mail address: oladeji.siyanbola@usm.edu (O.Q. Siyanbola).

https://doi.org/10.1016/j.ocemod.2022.102154
Received 1 August 2022; Received in revised form 29 October 2022; Accepted 26 November 2022
Available online 29 November 2022

(OBCs) is also important in mitigating discontinuities at the open boundaries (Marchesiello et al., 2001). Over the past decades, it has been a conventional practice to force regional models at the open boundaries with only sub-inertial fields and barotropic tides, and significant progress has been made towards developing appropriate OBCs for these motions (e.g., Flather, 1976; Marchesiello et al., 2001; Mason et al., 2010). However, in past studies of global internal tides and near-inertial waves (NIWs), it has been shown that these waves reach the coastal margins (e.g., Arbic et al., 2004; Simmons et al., 2004; Simmons and Alford, 2012; Waterhouse et al., 2014; Buijsman et al., 2016, 2020; Raja et al., 2022). Hence, it may also be important to include remote super-inertial internal gravity waves from global internal wave models, such as those cited above, at the regional model open boundaries.

It has been shown that the frequency spectra for regional models lack energy at super-tidal frequencies compared to observations (e.g., Kumar et al., 2019; Mazloff et al., 2020). To obtain better agreement between regional models and observations for the high-frequency continuum spectra, remotely generated internal wave forcing should be included at the open boundaries (Nelson et al., 2020). Nelson et al. (2020) and Gong et al. (2021) forced their regional simulations with high-frequency baroclinic fields acquired from the Massachusetts Institute of Technology general circulation model (MITgcm) LLC4320 global simulation (Rocha et al., 2016) and the High-resolution Empirical Tide (HRET) model (an altimeter-constrained internal tide model, Zaron, 2019), respectively. Nelson et al. (2020) found that the regional model frequency spectra agreed better with observations and the predictions of the Garrett and Munk (1975) spectrum up to 72 cycles per day (cpd), over what is seen in the global MITgcm LLC4320 simulation. Although these recent studies were able to obtain improved internal wave dynamics in their regional simulations, little attention was paid to the possibility of internal wave reflections at the open boundaries.

In this study, we provide evidence that energy build-up can occur in the domain due to internal tide reflections at the open boundaries. We look at how well Orlanski and Specified OBCs in combination with sponge layers mitigate boundary reflections of internal tides from the interior. We also assess how much the regional simulation with remote internal wave forcing improves when compared to observations. We choose to model the California Current System (CCS) region because it contains a strong internal tide generator, i.e., the Mendocino Escarpment, and the local internal wave energetics are affected by remotely generated internal tides, e.g., from Hawaii, and equatorward propagating NIWs. The eddy-rich CCS region is also an ideal site to study internal wave-eddy interactions (to be examined in a future paper). Lastly, the CCS region will be one of the sites for the SWOT Calibration and Validation (Cal/Val) experiment (Wang et al., 2018).

The layout of this paper is as follows. In Section 2, we describe the setup of our ocean circulation model, the boundary forcing, the open boundary conditions, the internal wave energy equations, the internal wave reflection analysis, and the validation datasets. We present our results on open boundary sensitivity analysis and model-data comparisons in Section 3. In Section 4, we discuss our findings. Finally, our conclusions are presented in Section 5.

2. Methodology

2.1. Model setup

We use the Regional Ocean Modeling System (ROMS) to simulate the internal wave energetics near the U.S. West Coast (USWC). ROMS is a 3-dimensional, primitive-equation, free-surface, and split-explicit regional ocean model. It makes use of an orthogonal curvilinear coordinate system in the horizontal plane and a topography-following (σ-) vertical coordinate system. Its forward–backward feedback time-stepping algorithms-based hydrodynamic computational kernel adopts a novel temporally averaging filter which ensures that slow baroclinic motions are not contaminated via aliasing of unresolved barotropic signals (Shchepetkin and McWilliams, 2005).

We use the ROMS configuration of Renault et al. (2021). Our ROMS regional simulations of the USWC feature a 4-km horizontal resolution, defined on a C-grid (Fig. 1). Our computational grid covers a significant portion of the USWC with the northernmost and southernmost vertices at 51.08°N and 22.71°N, respectively. The grid has 437 x 662 cells with a total area of approximately 1744 x 2644 km^2. The curvilinear grid is rotated at an angle of 28.7° in an anticlockwise manner relative to the eastward direction. Along the vertical direction, our regional simulations feature 60 σ-levels. The surface and bottom refinement stretching parameters (θ_s and θ_b) and pycnocline depth (h_c) are 6, 3 and 250 m, respectively (Shchepetkin and McWilliams, 2009).

The bathymetry for the regional simulations is taken from the 30-arc second resolution SRTM30-PLUS global topography grid (Becker et al., 2009). Except for the eastern boundary, the other three boundaries of our computational domain are open. To minimize depth mismatches at the open boundaries between the child and parent domains, we modify the child's topography using

$$h_{cm} = \alpha h_c + (1-\alpha)h_p, \tag{1}$$

where h_{cm}, h_c and h_p are the modified child grid, original child grid, and parent grid topography, respectively, and $0 \leq \alpha \leq 1$ over a narrow strip in the vicinity of the open boundaries. The parent grid is from a global HYbrid Coordinate Ocean Model (HYCOM) simulation, which is described in Section 2.1.1.

At the open boundaries, we specify high-frequency ($\omega > 0.67$ cpd) oceanic state variables extracted from the global HYCOM simulation. Oceanic low-frequency ($\omega < 0.67$ cpd) forcing fields are also specified at the open boundaries but they are obtained from a 12-km horizontal resolution ROMS simulation of the North-east Pacific. Low-frequency oceanic processes such as subtidal and mesoscale flows have temporal scales smaller than 1 cpd. To retain these motions and minimize the leakage of tidal energy to the subtidal band, we choose a 36 h (0.67 cpd) cutoff period. An extensive validation of the low-frequency fields for our domain is documented in Renault et al. (2021).

Atmospheric forcing for all our simulations is derived from a 6-km horizontal resolution uncoupled regional version of the Weather Research and Forecast (WRF) model (Skamarock et al., 2008; Renault et al., 2016). The WRF model uses a bulk formula (CORE, Large, 2006) with a parameterization of the current feedback to the atmosphere to estimate the surface evaporation and turbulent heat and momentum fluxes (Renault et al., 2020). We use hourly fields of 10-m wind, air temperature and humidity at 2 m, shortwave radiation, longwave radiation, and precipitation to force the ROMS simulations.

2.1.1. High-frequency boundary forcing

Remote high-frequency boundary forcing with $\omega > 0.67$ cpd for our regional simulations is derived from a simulation of global HYCOM (Bleck et al., 2002; Wallcraft et al., 2003) that includes realistic atmospheric and tidal forcing (e.g., Arbic et al., 2010, 2018; Shriver et al., 2012). HYCOM uses a hybrid vertical coordinate system with z-coordinates in the surface mixed layer, isopycnal layers in the open ocean and σ-coordinates over the coastal shelf. We force our ROMS domain with the global HYCOM expt_06.1 simulation (Buijsman et al., 2017, 2020), which has a nominal 8-km horizontal resolution and 41 hybrid layers in the vertical direction. The expt_06.1 bathymetry is based on the GEBCO_08 topographic database (https://www.gebco.net/). In conjunction with astronomical tidal forcing for the K_1, O_1, M_2, S_2, and N_2 tidal constituents, the non-data-assimilative expt_06.1 simulation utilizes realistic atmospheric forcing from the U.S. NAVY Global Environmental Model (NAVGEM) (Hogan et al., 2014). To account for the generation and dissipation of unresolved internal wave modes, expt_06.1 adopts a linear topographic wave drag scheme (Jayne and St. Laurent, 2001). Expt_06.1 has been exclusively validated against

moorings and altimetry (e.g., Arbic et al., 2018; Buijsman et al., 2020; Luecke et al., 2020).

Hourly model output of zonal and meridional velocity components u and v, temperature T, salinity S and sea surface height η for the period from 01 October, 2011 to 30 September, 2012 are obtained from HYCOM expt_06.1. We apply a 5th order Butterworth filter with a 36 h cutoff to extract the high-frequency components of these fields. For every time step, we employ ROMS pre-processing MATLAB tools for the horizontal and vertical interpolation of HYCOM fields to the ROMS open boundaries. Before forcing our model with the interpolated HYCOM fields, we ensure that the interpolation schemes perform satisfactorily (see Fig. 2). Our initialization file consists of ROMS low-frequency + HYCOM high-frequency oceanic state variables for 01 October, 2011. The weblinks to the MATLAB scripts for HYCOM to ROMS interpolation and all other relevant code scripts and datasets we use in this study are listed in the Acknowledgments.

2.1.2. Open boundary conditions

We conduct open boundary condition (OBC) sensitivity experiments that use Specified or Flather OBC (Flather, 1976; Mason et al., 2010) for barotropic velocities and sea surface height, and Specified or modified Orlanski OBC (Marchesiello et al., 2001) for baroclinic velocities and tracers. Based on the type of OBC adopted for barotropic–baroclinic fields, we categorize our simulations into three groups: Specified–Specified (SS), Flather–Specified (FS) and Flather–Orlanski (FO) simulations (Table 1).

The Flather OBC (Flather, 1976) is a radiation OBC based on the Sommerfeld condition (Chapman, 1985). The mathematical expression for the Flather OBC is

$$u_{\perp} = u_{\perp}^{ext} - \sqrt{\frac{g}{h}}\left(\eta - \eta^{ext}\right), \tag{2}$$

where $u_{\perp}$ is the normal barotropic velocity at the open boundary, $u_{\perp}^{ext}$ is the corresponding external $u_{\perp}$, η^{ext} is the external sea surface height, h is the depth of the water column and g is the acceleration due to gravity. The Flather OBC allows for mismatches between external barotropic information and interior solutions to be radiated out of the domain with the speed of a shallow-water surface gravity wave ($\sqrt{gh}$). A modified version of the Flather OBC suitable for staggered C-grid models such as ROMS, whose velocities and sea surface height are not co-located is extensively described in Mason et al. (2010).

The modified Orlanski OBC (Marchesiello et al., 2001) uses a radiative-relaxation numerical scheme. The mathematical expression for this adaptive numerical scheme is

$$\frac{\partial \phi}{\partial t} + c_x\frac{\partial \phi}{\partial x} + c_y\frac{\partial \phi}{\partial y} = -\frac{1}{\tau}(\phi - \phi^{ext}), \tag{3}$$

where ϕ represents any of the baroclinic variables/tracers in the domain, ϕ^{ext} is the corresponding external variable at the open boundaries, τ is the nudging coefficient, and c_x and c_y are the dominating wave phase speeds in the x and y directions, respectively. Eq. (4) is a modified version of the Orlanski OBC (Orlanski, 1976) with the addition of the nudging term $-\frac{1}{\tau}(\phi - \phi^{ext})$. During the active state (i.e., ingoing fluxes), ocean state variables in the nudging layer are relaxed towards the boundary forcing fields, and the open boundary switches to the radiative type when fluxes are directed outwards (i.e., passive). The open boundary becomes active when the computed normal phase speed c_x close to the boundary is negative and vice-versa when it is passive. We choose a relatively weak nudging coefficient for the passive state (τ_{out} = 30 days) and consider a stronger coefficient for the active state (τ_{in} = 0.005 day). We observe that $\tau_{in} > 0.01$ day limits the radiation of remotely generated internal waves at the open boundaries, i.e., under-specification, while we choose τ_{out} such that $\tau_{out} \gg \tau_{in}$ (Marchesiello et al., 2001).

Unlike the Flather and Orlanski OBCs that have radiation components in their numerical schemes, the Specified OBC is a clamped OBC. At the open boundaries, oceanic state variables at every time step are set to those of the parent grid for the Specified OBC.

$$\phi = \phi^{ext}, \tag{4}$$

where ϕ is any oceanic state variable and ϕ^{ext} is the corresponding external value.

For all our simulations, we add sponge layers at the open boundaries. Previous studies have shown that the inclusion of these buffer zones at the open boundaries can assist in preventing over-specification issues that may arise due to artificial reflections (e.g., Palma and Matano, 1998; Marchesiello et al., 2001; Nycander and Doos, 2003). To better understand the effect of the sponge layer on our simulations, we consider different sponge layer widths and horizontal viscosity values (A_h). The shape function for our sponge layers follows that of a half-cosine function with viscosity increasing from zero at the sponge interior to a maximum value at the open boundaries. Table 1 shows the sponge width and maximum viscosity values for all the simulations and nudging time scales for simulations with the Flather and modified-Orlanski OBCs, i.e., the FO simulations.

Table 1
Barotropic–baroclinic boundary conditions and energy terms for 12 regional simulations. Semidiurnal band (1.60 cpd $\leq \omega \leq$ 2.67 cpd), area-integrated, depth-integrated and time-mean (01 July–31 August, 2012) baroclinic Horizontal Kinetic Energy $\langle HKE \rangle$ and area-integrated and time-mean barotropic to baroclinic tide conversion $\langle C \rangle$ estimates are shown. $\langle .. \rangle$ denotes time-mean. Prefixes SS, FS and FO stand for Specified–Specified, Flather–Specified, and Flather–Orlanski simulations, respectively. FS800a is the only simulation without remote internal wave forcing.

Simulation	Sponge width (frac. of domain width)	A_h (m^2/s)	τ_{in}/τ_{out} (days)	$\langle HKE \rangle$ (PJ)	$\langle C \rangle$ (GW)
SS100	1/12	100	N/A	1.72	1.60
SS200	1/12	200	N/A	1.57	1.61
SS400	1/12	400	N/A	1.46	1.60
SS600	1/30	600	N/A	1.41	1.56
SS800	1/30	800	N/A	1.34	1.56
FS600	1/30	600	N/A	1.59	2.04
FS800a	1/30	800	N/A	0.89	1.87
FS800b	1/30	800	N/A	1.59	2.08
FO100	1/12	100	0.005/30	1.85	2.00
FO200	1/12	200	0.005/30	1.73	2.00
FO300	1/12	300	0.005/30	1.64	2.00
FO600	1/30	600	0.005/30	1.62	2.00

2.2. Internal tide energetics

To examine the internal tide generation, radiation, and dissipation within our computational domain, we apply the depth-integrated and time-mean baroclinic energy balance equation (Carter et al., 2008; Kelly et al., 2010; Kang and Fringer, 2012)

$$\left\langle \frac{\mathrm{d}E}{\mathrm{d}t} \right\rangle + \langle \nabla_H \cdot \mathbf{F} \rangle = \langle C \rangle - \langle D \rangle, \tag{5}$$

where E represents the total depth-integrated baroclinic energy, $\nabla_H \cdot \mathbf{F}$ is the pressure flux divergence, C is the barotropic to baroclinic tide conversion, and D is dissipation. $\nabla_H = \frac{\partial}{\partial x}\hat{i} + \frac{\partial}{\partial y}\hat{j}$ and $\langle .. \rangle$ represents time averaging.

The total depth-integrated baroclinic energy E is the sum of the depth-integrated baroclinic horizontal kinetic energy (HKE) and the available potential energy (APE). For a water column of depth h, HKE and APE can be expressed as

$$HKE = \frac{\rho_0}{2}\int_{-h}^{0}\left(u'(z)^2 + v'(z)^2\right)\mathrm{d}z, \tag{6}$$

$$APE = \frac{\rho_0}{2}\int_{-h}^{0} N(z)^2\xi(z)^2\mathrm{d}z, \tag{7}$$

where $\rho_0 = 1027.4$ kg/m^3, $\mathbf{u}'(z) = u'(z)\hat{i} + v'(z)\hat{j}$ is the baroclinic velocity vector, $N(z)$ is the buoyancy frequency, and $\xi(z)$ is the isopycnal

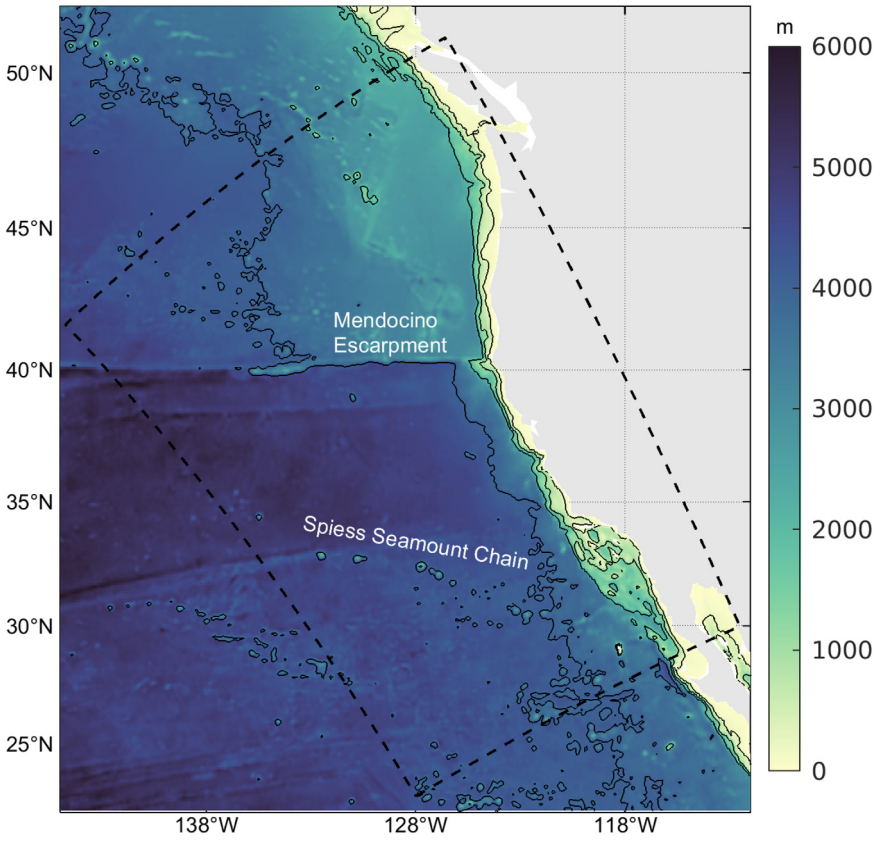

Fig. 1. Bathymetry near the U.S. West Coast. The black continuous lines are the 200, 1000, 2000, and 4000 m seafloor depth contours and the dashed black polygon represents the extent of our ROMS model computational domain.

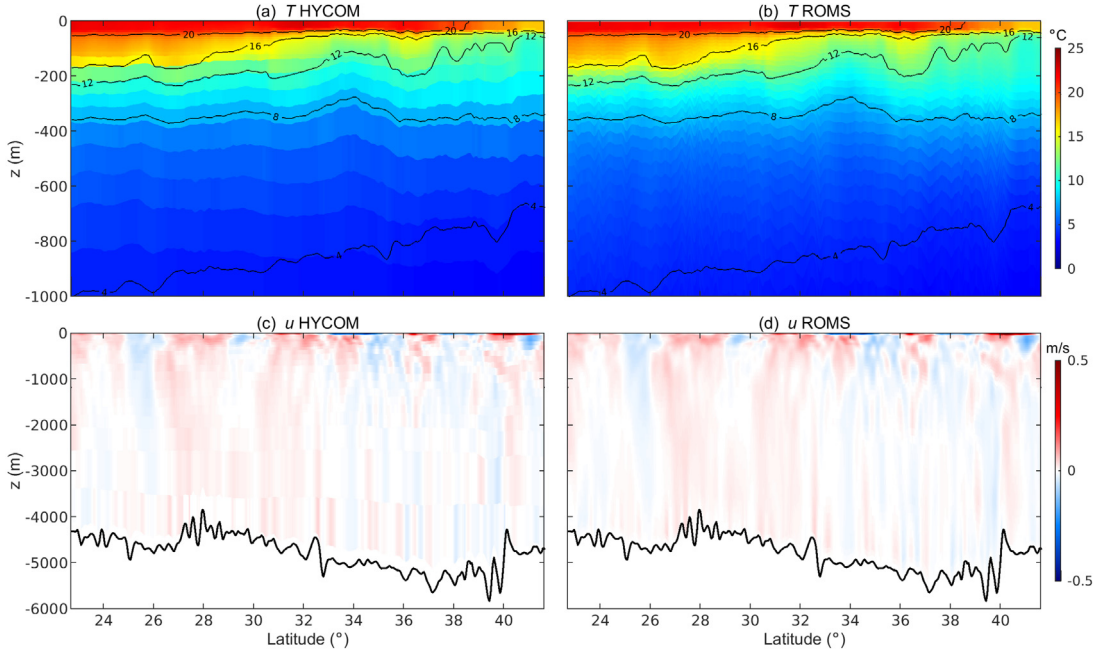

Fig. 2. Snapshots of temperature T (top 1000 m depth) and velocity u at 01:00:00 on 01 October, 2011 along the western boundary for HYCOM (a, c) and ROMS (b, d), respectively. This figure shows that the interpolated fields of ROMS agree well with the original HYCOM fields.

displacement at depth z. The baroclinic velocities are defined such that

$$\mathbf{u}' = \mathbf{u} - \mathbf{U}, \tag{8}$$

where $\mathbf{u}$ is the total velocity, and $\mathbf{U} = \frac{1}{h+\eta}\int_{-h}^{\eta}\mathbf{u}(z)\mathrm{d}z$ is the barotropic velocity. We compute the depth-integrated baroclinic flux as (Nash et al., 2005)

$$\mathbf{F} = \int_{-h}^{0}\mathbf{u}'(z)p'(z)\mathrm{d}z, \tag{9}$$

where p' is the pressure perturbation. The depth integration of the baroclinic velocities and pressure perturbations are equal to 0. We compute barotropic to baroclinic tide conversion as

$$C = p'(z=-h)\mathbf{U}\cdot\nabla_H(-h), \tag{10}$$

where $p'(z=-h)$ is the near-bottom pressure perturbation. We do not compute dissipation explicitly; it is the residual of the sum of all other terms in Eq. (5).

2.3. Estimation of internal wave reflections

We quantify internal wave reflections at the open boundaries with a Discrete Fourier Transform (DFT) technique, which separates ingoing and outgoing waves (Gong et al., 2021), in combination with an internal wave energy budget of the sponge layer. In the Appendix, we illustrate the good performance of the DFT technique on an analytical mode 1 standing wave and on a complex wave field from HYCOM. We apply the DFT technique to u', v' and p' along transects perpendicular to the open boundaries and repeat this process for the 60 vertical layers. Each transect along which the DFT technique is applied is 320 km long and equals two mode 1 M_2 internal tide wavelengths in the USWC (Buijsman et al., 2020). The total baroclinic flux, can be expressed as

$$\begin{aligned}\mathbf{F} &= \int_{-h}^{0}(p'_{in}+p'_{out})(\mathbf{u}'_{in}+\mathbf{u}'_{out})\mathrm{d}z \\ &= \underbrace{\int_{-h}^{0}p'_{in}\mathbf{u}'_{in}\mathrm{d}z}_{F_{in}} + \underbrace{\int_{-h}^{0}p'_{out}\mathbf{u}'_{out}\mathrm{d}z}_{F_{out}} + \underbrace{\int_{-h}^{0}p'_{in}\mathbf{u}'_{out}\mathrm{d}z + \int_{-h}^{0}p'_{out}\mathbf{u}'_{in}\mathrm{d}z}_{F_{cross}},\end{aligned} \tag{11}$$

where F_{in} and F_{out} represent the depth-integrated ingoing and outgoing flux components, respectively, and the last two terms are the cross terms F_{cross}.

A schematic showing the different fluxes that contribute to the semidiurnal internal wave energy budget of the sponge layer is presented in Fig. 3. We obtain F_{in} and F_{out} by depth-integrating unidirectional ingoing and outgoing fluxes at the sponge interior edges. We do not consider the cross terms in Eq. (11) because they are very small after time averaging. F_{HYCOM} represents the depth-integrated unidirectional ingoing flux from HYCOM, F_{con} is the barotropic to baroclinic tide conversion in the sponge layer normalized by the length of the interior sponge boundary, and F_r is the depth-integrated unidirectional reflected flux into the interior of the domain.

In the absence of reflections at the open boundaries, neglecting dissipation of F_{HYCOM} and assuming that the flux due to the barotropic to baroclinic tide conversion in the sponge layer propagates into the interior of the domain, we expect $\langle F_{out}\rangle$ to balance $\langle F_{HYCOM}\rangle + \langle F_{con}\rangle$. In this study, we treat the excess in $\langle F_{out}\rangle$ as reflected flux and a deficit in $\langle F_{out}\rangle$ as an indication of the over-damping of F_{HYCOM} due to the sponge layer. Because the sponge layer is expected to dampen some of the internal tide signals and we are not sure what fraction of the dissipation in this buffer zone comes from F_{HYCOM}, F_{in}, and/or the local conversion, we create ranges for our reflection estimates ($\langle F_{r,1}\rangle \le \langle F_r\rangle \le \langle F_{r,4}\rangle$) based on the following assumptions:

1. All dissipation in the sponge layer comes from F_{in}: $\langle F_{r,1}\rangle = \langle F_{out}\rangle - \langle F_{HYCOM}\rangle - \langle F_{con}\rangle$
2. F_{con} is completely dissipated in the sponge layer and the remaining dissipation in the sponge layer is from F_{in}: $\langle F_{r,2}\rangle = \langle F_{out}\rangle - \langle F_{HYCOM}\rangle$
3. One-third of the dissipation in the sponge layer is from F_{HYCOM}: $\langle F_{r,3}\rangle = \langle F_{out}\rangle - \langle F_{con}\rangle - (\langle F_{HYCOM}\rangle - \frac{1}{3}\langle D\rangle)$
4. F_{con} is completely dissipated in the sponge layer and one-third of the remaining dissipation in the sponge layer is from F_{HYCOM}: $\langle F_{r,4}\rangle = \langle F_{out}\rangle - (\langle F_{HYCOM}\rangle - \frac{1}{3}(\langle D\rangle - \langle F_{con}\rangle))$

We choose one-third of the dissipation in the third and fourth assumptions because F_{in} is expected to travel twice the distance than F_{HYCOM} through the sponge layer before entering the interior. We compute the reflection coefficient as $\lambda = \langle F_r\rangle/\langle F_{in}\rangle$.

2.4. Model validation

A year long solution of the simulation judged "best" is compared to observations after conducting the sensitivity analysis of the boundary forcing. To quantify the improvements in model-data comparisons with high-frequency baroclinic forcing, we also compare the simulation without remote internal wave forcing to observations.

2.4.1. Barotropic tides

We validate the simulated barotropic tides in our domain with the TPXO9-atlas (Egbert et al., 1994; Egbert and Erofeeva, 2002). We conduct harmonic analysis with the UTide MATLAB package (Codiga, 2011) on a year-long ROMS η time series to extract the O_1, K_1, N_2, M_2 and S_2 tidal constituents.

We compute root mean square errors ($RMSE$s) for tidal elevations η. The $RMSE$ expression considers errors due to deviations in both simulated amplitude A and phase ϕ with respect to those of TPXO (Shriver et al., 2012), i.e.,

$$RMSE = \sqrt{\frac{1}{2}\left(\left(A_R\cos\phi_R - A_X\cos\phi_X\right)^2 + \left(A_R\sin\phi_R - A_X\sin\phi_X\right)^2\right)}, \tag{12}$$

where subscripts 'R' and 'X' stand for ROMS and TPXO, respectively. To determine how large the errors are relative to the simulated tidal signals, we estimate the area-averaged coefficient of determination (Arbic et al., 2004)

$$R^2_\eta = \left(1 - \left(\frac{\{RMSE\}}{\sqrt{\{\sigma^2_{\eta,X}\}}}\right)^2\right) * 100\%, \tag{13}$$

where $\sigma^2_{\eta,X} = 0.5A^2_X$ is the TPXO sea surface height variance and $\{..\}$ represents area-averaging.

2.4.2. Moorings

We validate our model simulations with Eulerian temperature and velocity measurements of the Global Multi-Archive Current Meter Database (GMACMD, Scott et al., 2010; Luecke et al., 2020). We also consider temperature mooring instruments of the California Current Ecosystem (CCE) database (Ohman et al., 2013). For the GMACMD moorings, we exclude mooring instruments that fall outside our domain and in the sponge layers. We also eliminate moorings at locations where the depth of the sea floor is < 500 m. None of the CCE moorings lie in the sponge or shallow regions. The geographical locations and the distribution of the mooring instruments with depth in our domain are shown in Fig. 4. A total of 483 (334-velocity and 149-temperature) mooring instruments are considered. The depth for the moorings ranges from 6.1 to 4300 m and approximately 58% of these moorings lie in the upper 1000 m of the water column.

We perform frequency spectral analysis on the mooring temperature and velocity datasets. To achieve smooth frequency spectra, we divide each time series into 30 days-long segments with 50% overlaps. Prior

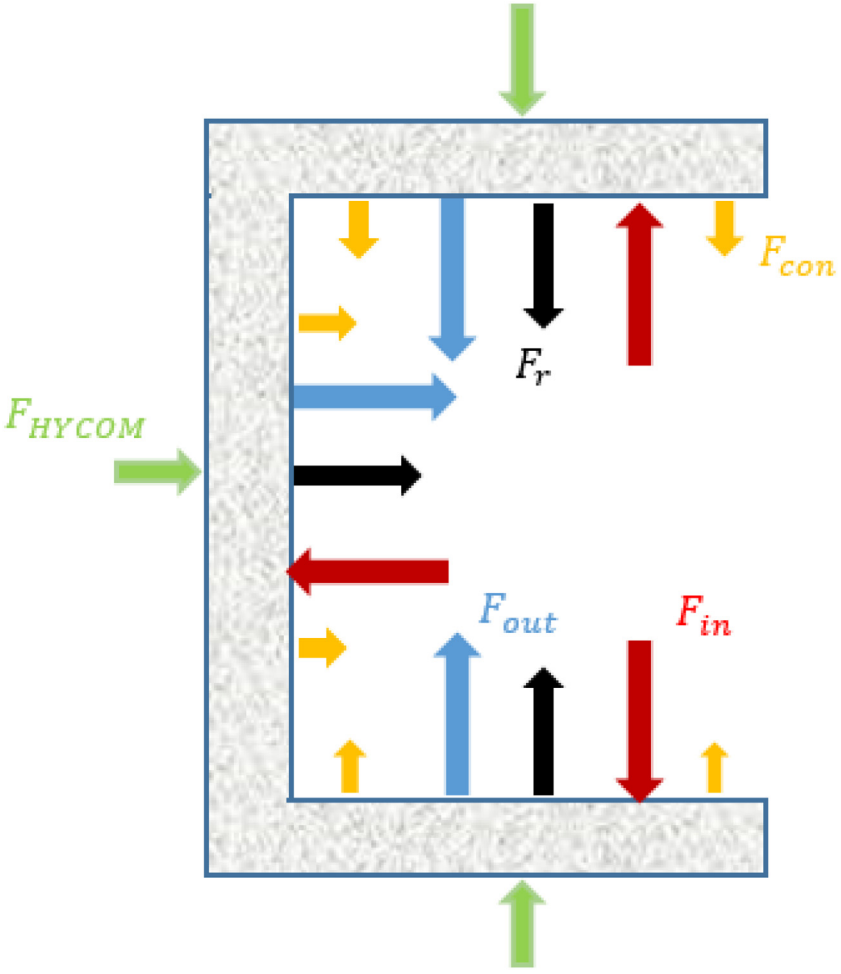

Fig. 3. Schematic of fluxes as part of the sponge layer baroclinic energy budget. F_{HYCOM} represents the unidirectional incoming flux from HYCOM, F_{in} is the unidirectional flux into sponge from the interior of the domain, F_{out} is the unidirectional flux out of sponge, F_{con} represents the barotropic to baroclinic tide conversion normalized by the interior sponge boundary length, and F_r is the unidirectional reflected flux.

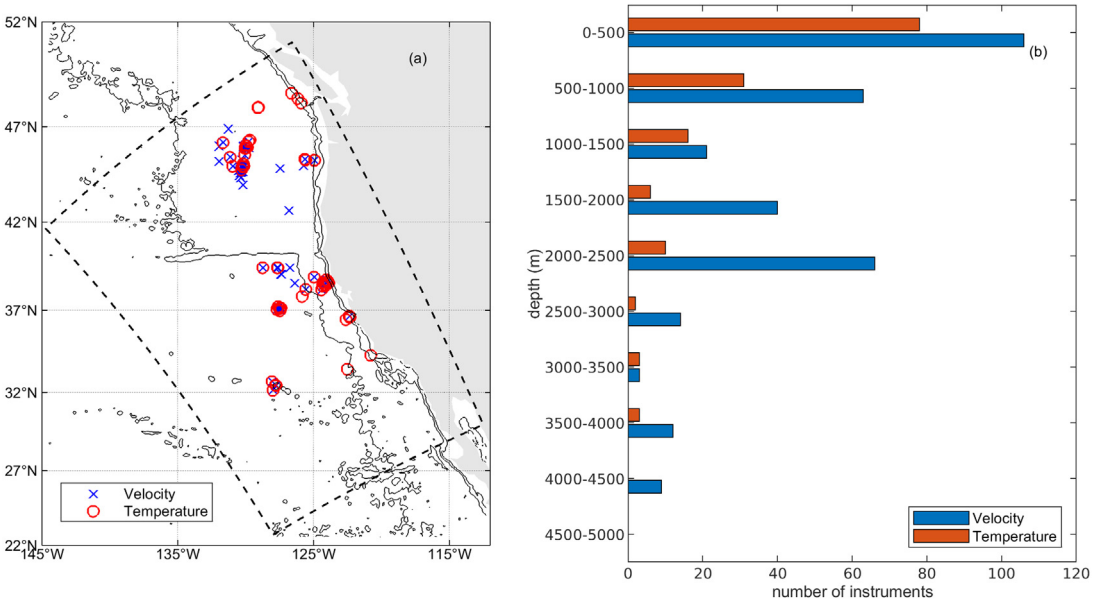

Fig. 4. (a) Geographical locations of historical moored measurements of temperature and velocity, and (b) distribution of mooring instruments with depth. The dashed black polygon in (a) depicts the extent of our ROMS model computational domain. Thin continuous black lines in (a) are the same depth contours as in Fig. 1.

to applying the Fast Fourier Transform (FFT), we remove the mean and the linear trend and we multiply each detrended time series by a Tukey window with a taper length to total length ratio of 0.2. To preserve total variance, we apply a variance preserving correction factor. We then compute temperature variance (σ_T^2) and the velocity variance (σ_{vel}^2), and integrate over three frequency bands: semidiurnal (1.86–2.05 cpd), super-tidal (2.06–12 cpd), and near-inertial (0.9f–1.74 cpd; f is the local Coriolis frequency). For the near-inertial band, we account for remotely generated near-inertial waves from the Gulf of Alaska, whose northernmost latitude of $\sim 60.41°$N corresponds to $f = 1.74$ cpd. The expressions for temperature and velocity variance are

$$\sigma_T^2 = \frac{2\Delta t}{n} \int_{\omega_{min}}^{\omega_{max}} |\widehat{T(\omega)}|^2 \mathrm{d}\omega, \tag{14}$$

$$\sigma_{vel}^2 = \frac{\Delta t}{n} \int_{\omega_{min}}^{\omega_{max}} \left| \widehat{U(\omega)^2} + \widehat{V(\omega)^2} \right| \mathrm{d}\omega, \tag{15}$$

where n is the number of data points in a time series spaced at uniform Δt time intervals, $\widehat{T(\omega)}$, $\widehat{U(\omega)}$, and $\widehat{V(\omega)}$ are the Fourier coefficients for temperature, eastward velocity u, and northward velocity v, respectively, and ω_{min} and ω_{max} represent the lower and the upper frequency limits for each frequency band.

For model-mooring comparisons, we use the same statistics as adopted by Luecke et al. (2020). For all frequency bands, we compute the ratio of the mean of the model variance to that of the moorings for velocity and temperature

$$\gamma = \frac{\{\sigma_{\mathrm{M}}^2\}}{\{\sigma_{\mathrm{O}}^2\}}, \tag{16}$$

where subscripts M and O refer to the simulated and observed variable, respectively. Lastly, we compute correlation coefficients r between simulations and observations.

2.4.3. Altimetry

Finally, we compare baroclinic M_2 η amplitudes of one-year ROMS simulations with those extracted from a 17-year long altimetry dataset, which was used by Shriver et al. (2012) and Buijsman et al. (2020) in their global studies. We extract complex harmonic η amplitudes for M_2 tides from the ROMS simulations using the UTide package. Following Shriver et al. (2012), we interpolate the complex amplitudes to along-track positions that fall in our domain. We then apply a 50–400 km bandpass filter along ascending and descending tracks for ROMS and altimeter datasets to extract low-mode internal tide complex amplitudes. We apply the spatially varying correction factor of Buijsman et al. (2020) to the ROMS internal tide amplitudes. The variance correction factor is the ratio of the equilibrium stationary variance to that of the simulated time series. Because the stationary internal tide variance obtained from a time series decreases with its duration (Ansong et al., 2015), the variance correction factor is necessary to allow for the comparison of the stationary internal tide signals of the one year long ROMS simulations with those obtained from the much longer altimetry record. The average variance correction factor for our domain is 0.81. Finally, we compute root mean square amplitude ($RMSA$) for both altimetry and the ROMS simulations, and then ratios and correlation coefficient.

3. Results

3.1. High-frequency baroclinic fluxes at the open boundaries

We compute the high-frequency ($\omega > 0.67$ cpd), depth-integrated and time-averaged HYCOM baroclinic fluxes at the open boundaries for the period 01 October, 2011 to 30 September, 2012 (Fig. 5a). Approximately 541 MW (93 W/m) of net high-frequency baroclinic power enters our computational domain, which is of similar magnitude as that of Mazloff et al. (2020). Our northern (403 MW; 210 W/m) and western (270 MW; 102 W/m) boundaries act as sources while the southern boundary is a sink (−132 MW; −87 W/m) of high-frequency baroclinic energy.

At the western and northern boundaries, respectively 177 W/m and 93 W/m of net semidiurnal internal tidal flux enters the domain. One of the origins of these remote fluxes is the Hawaiian island chain to the west of our domain. This is shown with the presence of internal tidal beams crossing the western/northern boundaries (Fig. 5a). The southern boundary acts as a sink of approximately 37 W/m of semidiurnal internal tidal flux.

As expected, our analysis shows equatorward propagation of NIWs (Fig. 5a); NIWs (0.9f–1.74 cpd) enter our domain through the northern boundary and exit via the western and southern boundaries. NIWs contribute more than 50% of the net high-frequency baroclinic fluxes at the northern (117 W/m) and southern (−50 W/m) boundaries. This shows that NIWs make up a significant fraction of the high-frequency barolinic forcing. At the western boundary, 75 W/m of NIWs flux exits our domain.

3.2. Generation, radiation, and dissipation of semidiurnal internal tides

The spatial pattern of the time-mean (01 July, 2012–31 August, 2012) semidiurnal internal tide generation in our domain for FS800a, without remote internal wave forcing, is shown in Fig. 6a. The Mendocino Escarpment (Fig. 1) is an important generation site, featuring $\langle C \rangle > 10$ mW/m^2. Other rough topographic features such as the continental margin and the Spiess seamount chain (Fig. 1) contribute to the total area-integrated conversion of 1.87 GW (0.61 mW/m^2) in our domain (Table 1). Areas with $\langle C \rangle < 0$ are regions where the barotropic velocity and the near-bottom baroclinic pressure field are out of phase. With remote internal wave forcing at the open boundaries, internal tide generation in the interior of the domain increases. Area-integrated conversion for the twin solution FS800b, with remote internal wave forcing, is 2.08 GW (0.68 mW/m^2). This is an indication that the remote internal tides alter the magnitude and/or phase of the near-bottom pressure perturbation field in the domain Buijsman et al. (2010), Kelly and Nash (2010), Kerry et al. (2013).

The radiation of internal tides away from the generation sites in our domain is determined by computing the time-mean flux divergence $\langle \nabla_H \cdot \mathbf{F} \rangle$. The spatial pattern of the time-mean flux divergence in Fig. 6b resembles that of conversion, and is positive in areas of strong generation. In some locations, the flux divergence is negative, e.g., in the sponge layer and on the continental margin. This is an indication that the internal tide dissipation exceeds local generation.

We estimate internal tide dissipation as the residual of conversion and flux divergence, following Eq. (5). The contributions of the time-mean energy tendency and advection terms are very small (not shown). The plot of time-mean internal tide dissipation (Fig. 6c) demonstrates that dissipation occurs throughout the domain, with higher dissipation on the continental margin and in the sponge layer. The internal tide dissipation in the sponge layer increases towards the open boundaries, in agreement with the increase in horizontal viscosity (see Section 2.1.2).

3.3. Sensitivity of internal wave energetics to open boundary conditions

In this section, we conduct an OBC sensitivity analysis for the semidiurnal band (1.60 cpd $\leq \omega \leq$ 2.67 cpd). We choose 01 July, 2012–31 August, 2012 for our analysis because the semidiurnal internal tides that enter the domain from Hawaii are strongest and NIWs are weakest during these months. We initialized our trial simulations on 01 June, 2012, allowing enough time for spin up.

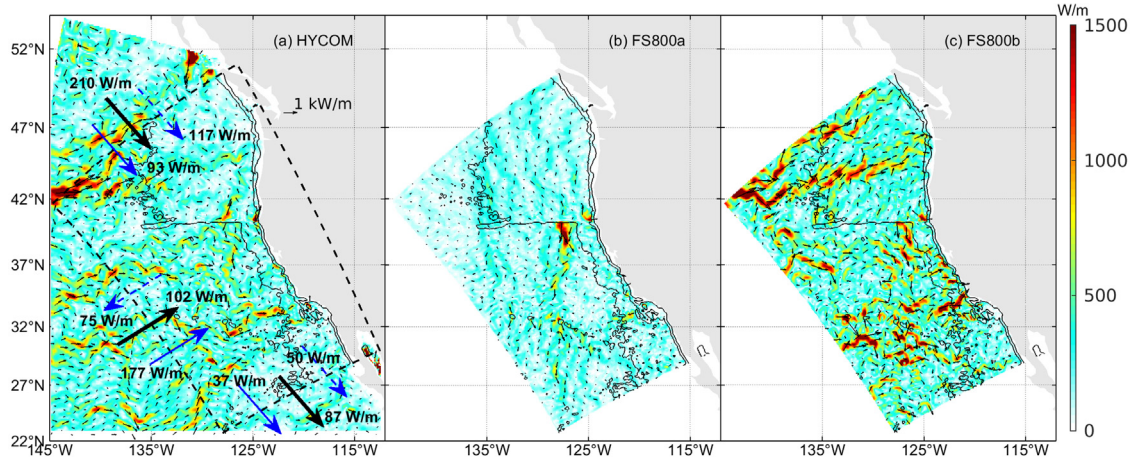

Fig. 5. Depth-integrated and time-mean (01 July–31 August, 2012) semidiurnal band (1.60 cpd $\leq \omega \leq$ 2.67 cpd) baroclinic fluxes for (a) HYCOM, (b) ROMS simulation without (FS800a) and, (c) ROMS simulation with (FS800b) remote high-frequency baroclinic boundary forcing. The super-imposed polygon in (a) is the extent of our ROMS model computational domain. The black solid, blue solid and dashed arrows indicate the direction of the boundary-integrated and time-mean total high-frequency, semidiurnal and NIW ($0.9f \leq \omega \leq$ 1.74 cpd) fluxes, respectively. Thin continuous black lines in (a) to (c) are the same depth contours as in Fig. 1.

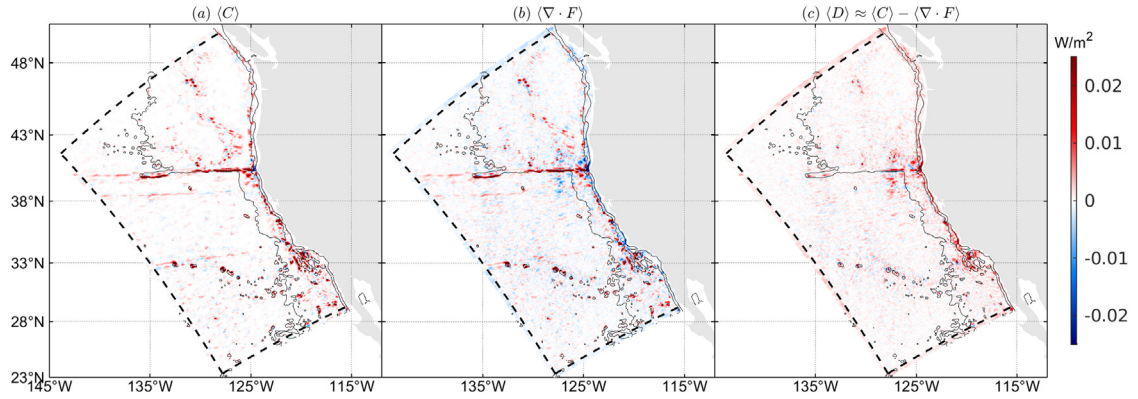

Fig. 6. Time-mean (01 July–31 August, 2012) (a) barotropic to baroclinic energy conversion, (b) pressure flux divergence, and (c) dissipation for FS800a without remote internal wave forcing. The black dashed lines mark the sponge interior boundary. Thin continuous black lines in (a) to (c) are the same depth contours as in Fig. 1.

3.3.1. Interior energetics

The differences in semidiurnal baroclinic energy flux magnitude and direction between simulations without (FS800a) and with (FS800b) remote internal tides are large (Fig. 5b and c). With remote semidiurnal baroclinic forcing, our domain becomes more energetic. We list the area-integrated, depth-integrated, and time-mean baroclinic $\langle HKE \rangle$ estimates for the 11 boundary sensitivity simulations and that of FS800a in Table 1. We do not include the sponge layer in the computation of the reported $\langle HKE \rangle$ values. To ensure an apples-to-apples comparison between the simulations, we mask cells that fall within the larger sponge width, i.e., 1/12th of the domain's width, before computing the area-integrated $\langle HKE \rangle$. Of all the simulations, FS800a has the lowest $\langle HKE \rangle$ estimate. We record the highest baroclinic $\langle HKE \rangle$ estimates for FO100 and SS100, which feature the weakest sponge viscosity. As we increase sponge viscosity and/or sponge width, the baroclinic $\langle HKE \rangle$ is reduced in the interior of the domain. The question is: are we reducing reflections in our domain and/or are we over-damping the incoming HYCOM fluxes at the open boundaries with increasing sponge viscosity and/or sponge width? We provide an answer to this question by estimating reflection coefficients in Section 3.3.2.

For simulations with similar sponge width and viscosity, we obtain smaller $\langle HKE \rangle$ and $\langle C \rangle$ estimates for the SS group as compared to the FS and FO simulations (Table 1). We show in Fig. 7 the spatial $\langle HKE \rangle$ maps for SS600, FS600, and the difference between them. Although SS600 and FS600 have the same sponge width, viscosity and OBC for the baroclinic mode, SS600 is less energetic over the entire domain as compared to FS600. Simulations with Specified OBC for the barotropic fields have smaller conversion rates as compared to the simulations with Flather OBC. We demonstrate in Section 3.4.1 that the barotropic tide signals are more in agreement with TPXO for Flather OBC than for Specified OBC.

3.3.2. Internal tide reflections at the open boundaries

To test our hypothesis that the increased $\langle HKE \rangle$ corresponding to lower sponge viscosities (Table 1) is due to increased reflections, we carry out a baroclinic energy budget analysis of the sponge layer. In Table 2, we list the fluxes as defined in Section 2.3 that contribute to the sponge's baroclinic energy budget for all the 11 trial simulations with remote internal wave forcing. We also include dissipation estimates in the sponge layers. For simulations with similar OBCs and sponge widths, e.g., SS100–SS400, the dissipation increases in the sponge layer with increasing viscosity values. SS600 has a smaller dissipation estimate than SS400 because the latter has a wider sponge (Tables 1 and 2, Fig. 8a). Similarly, the dissipation in FO300 is larger than in FO600 because FO300 has a larger sponge width than FO600. As the dissipation increases for increasing viscosity, $\langle F_{out} \rangle$ decreases (Table 2, Fig. 8b). For all 11 trial simulations with remote internal wave forcing, $\langle F_{out} \rangle > \langle F_{HYCOM} \rangle + \langle F_{con} \rangle$, where $\langle F_{HYCOM} \rangle = 229.6$ W/m. This indicates that interior energy is reflected in these simulations, i.e., $\langle F_r \rangle \neq 0$. As with $\langle F_{out} \rangle$, the reflected flux $\langle F_r \rangle$ decreases with increasing sponge viscosity (Fig. 8c).

The impact of the increased viscosity on energy fluxes near the boundaries is shown in Fig. 9. At the open boundaries, FO100 has

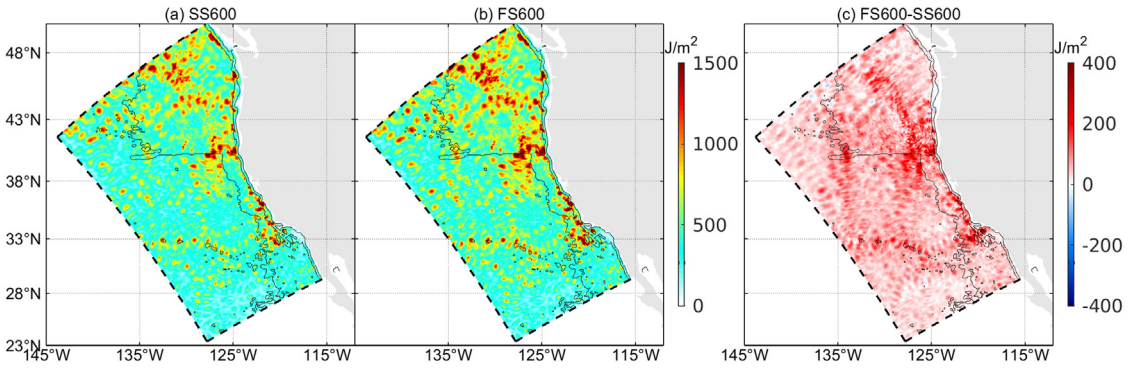

Fig. 7. Depth-integrated and time-mean (01 July–31 August, 2012) semidiurnal band $\langle HKE \rangle$ for (a) SS600, (b) FS600, and (c) their difference, FS600-SS600. The dashed lines mark the sponge interior boundary. Thin continuous black lines in (a) to (c) are the same depth contours as in Fig. 1.

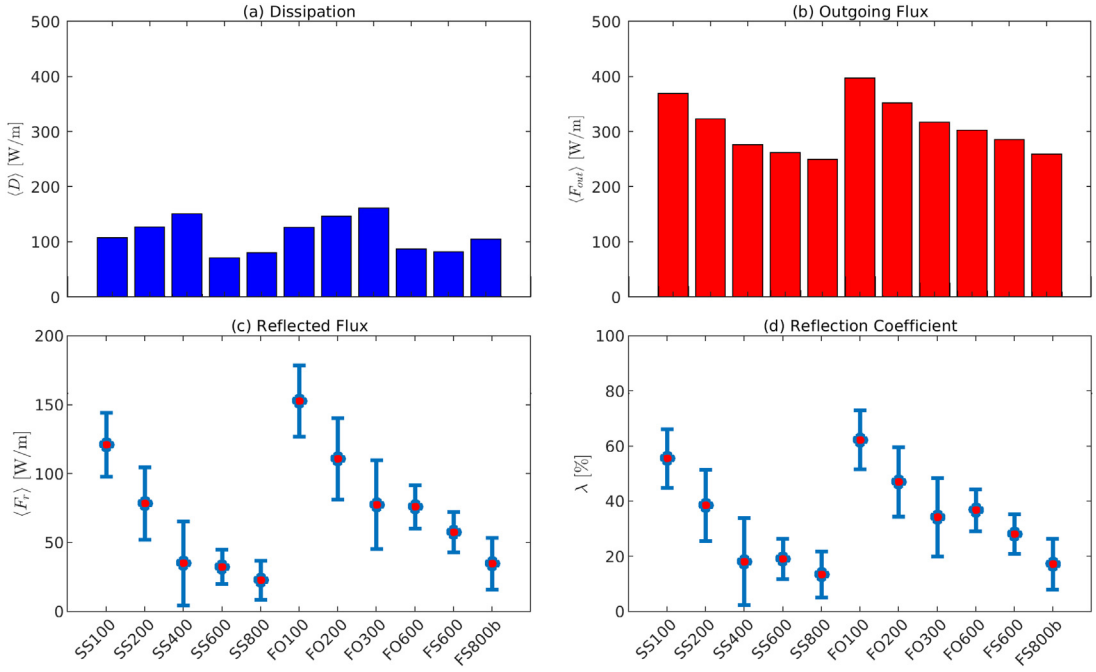

Fig. 8. Energy budget of the sponge layer for all 11 boundary sensitivity simulations with remote internal wave forcing. (a) Dissipation $\langle D \rangle$, (b) $\langle F_{out} \rangle$, (c) $\langle F_r \rangle$ and (d) reflection coefficient (λ). Red dots in (c) and (d) represent the mean over the range of $\langle F_{r,1} \rangle$ to $\langle F_{r,4} \rangle$ and the corresponding λ estimates, while the whiskers depict one standard deviation from the mean.

higher depth-integrated fluxes propagating into the domain compared to FO600 — an indication of higher internal tide reflections due to smaller sponge viscosity. In Fig. 9c, there is more northeastward propagation of internal tides in FO100 as compared to FO600 almost everywhere in the domain. This implies that reflected internal waves from the western boundary propagate into the domain over large distances. Similarly, in Fig. 9f, FO100 features more southeastward propagation of internal tides from the northern boundary and more northwestward propagation of internal tides from the southern boundary as compared to FO600.

Although SS600 and FS600 have similar boundary properties, i.e., sponge width, viscosity and Specified OBC for the baroclinic mode, FS600 has stronger reflections (Fig. 8c). This is in agreement with our finding in the preceding section that larger surface tides and barotropic to baroclinic conversion is obtained for Flather OBC as compared to Specified OBC for barotropic tides.

We observe that Orlanski OBC causes more reflections than the Specified OBC (Table 2). This is an indication that the Orlanski OBC is not doing a better job in handling the highly dispersive outgoing wave packets from the interior of the domain. To illustrate that reflections are enhanced in FO600, we show the spatial maps of $\langle HKE \rangle$ for FS600, FO600, and the difference between them in Fig. 10. While the $\langle HKE \rangle$ patterns for FS600 and FO600 are similar (Fig. 10a and b), FO600 is slightly more energetic in the majority of the domain (Fig. 10c). We compute a difference of 1619.7–1591.8 = 27.9 TJ (9.2 J/m^2) of area-integrated (averaged) $\langle HKE \rangle$ between FO600 and FS600 (see Table 1).

Similar to $\langle F_r \rangle$, λ diminishes with increasing sponge viscosity for simulations with a constant sponge width and similar OBCs (Table 2, Fig. 8d). λ attains its largest value of 73% for FO100. SS400 has the smallest reflection coefficient of 2.5%, but the barotropic tides are less accurate for Specified OBC than for Flather OBC as will be discussed in Section 3.4.1. λ is higher for simulations with baroclinic Orlanski OBC as compared to the simulations with Specified OBC. We select FS800b as the best trial simulation because: (1) the barotropic tides are well predicted with Flather OBC and (2) internal tide reflections at the open boundaries are minimized ($\lambda = 17.5 \pm 9.9\%$) when we use a combination of Specified OBC for the baroclinic mode and a 58-km wide sponge layer with a maximum viscosity of 800 m^2/s.

From our reflection analysis, we conclude that it is necessary to include sponge layers at the open boundaries of internal-wave-resolving regional simulations to minimize reflections of internal waves from the

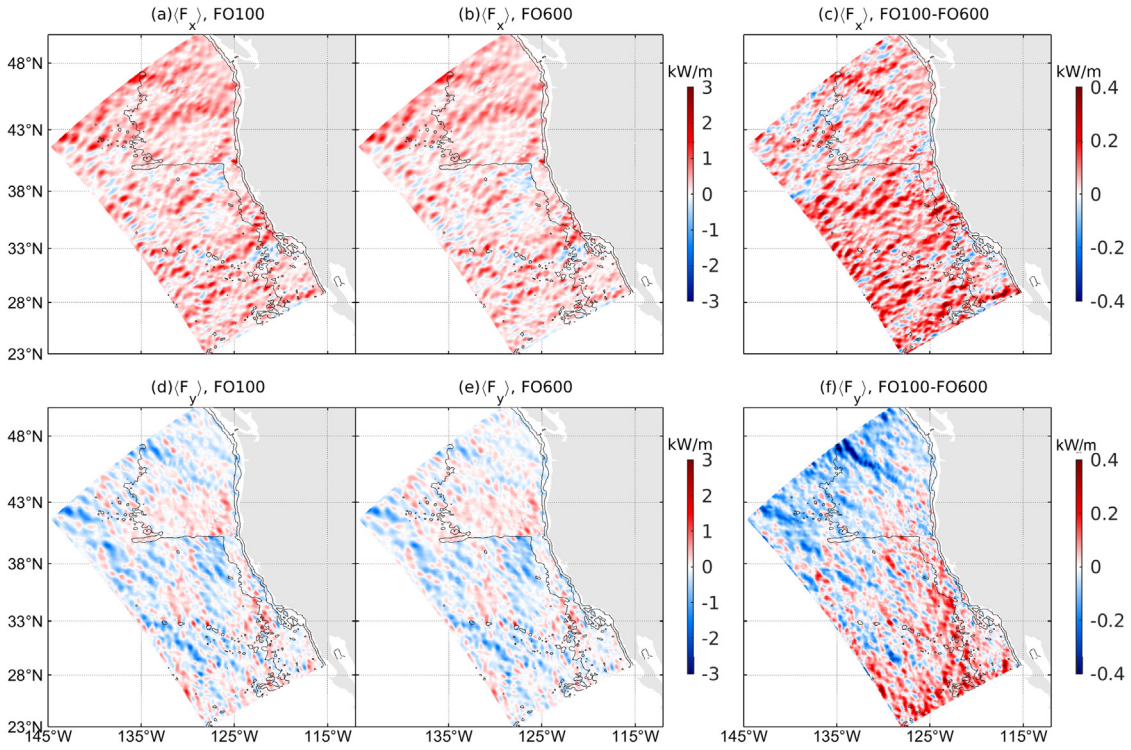

Fig. 9. Depth-integrated and time-mean (01 July–31 August, 2012) semidiurnal baroclinic fluxes along the rotated x-axis (first row) and along the rotated y-axis (second row) for FO100 (first column), FO600 (second column) and the difference between FO100 and FO600 (third column). Positive (negative) values in (a), (b) and (c) indicate N-E (S-W) propagation. Positive (negative) values in (d), (e) and (f) indicate N-W (S-E) propagation. The rotated x-axis is at angle of 28.7° in an anticlockwise manner relative to east. Thin continuous black lines in (a) to (f) are the same depth contours as in Fig. 1.

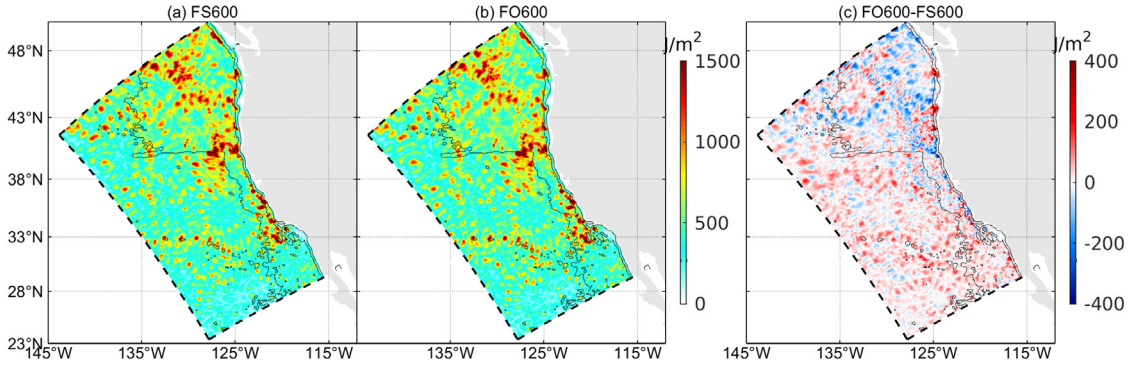

Fig. 10. Depth-integrated and time-mean (01 July–31 August, 2012) semidiurnal band $\langle HKE \rangle$ for (a) FS600, (b) FO600 and (c) their difference, FO600-FS600. The dashed lines mark the sponge interior boundary. Thin continuous black lines in (a) to (c) are the same depth contours as in Fig. 1.

interior when specifying remote internal waves at the open boundaries. However, one should be careful to prevent over-damping of the remote internal wave signals.

3.4. Model-data comparisons

In this section, we compare our best simulation (FS800b, λ = 17.5 ±9.9%) and its twin simulation, with the same parameters but without remote internal wave forcing (FS800a), with observations. We validate these simulations for the period from 08 October, 2011 to 30 September, 2012. We do not consider the first seven days after initialization (01 October–07 October, 2011) to exclude any barotropic and/or baroclinic spin-up effects. We present model validation results using TPXO in Section 3.4.1, moorings in Section 3.4.2, and altimetry in Section 3.4.3.

3.4.1. Simulated barotropic tide validation using TPXO

The area-averaged $RMSE$ (Eq. (12)) and the coefficient of determination R^2_η (Eq. (13)) for O_1, K_1, N_2, M_2 and S_2 tides for FS800b are given in Table 3. We obtain similar estimates for FS800a because it also uses a Flather OBC for the barotropic tides. Overall, the diurnal tidal constituents have the smallest area-averaged $RMSE$s and the largest R^2_η compared to the semidiurnal tides. The highest area-weighted surface tidal error is for the M_2 tidal constituent (3.40 cm), whereas, S_2 has the smallest coefficient of determination of 97.71 %.

The co-tidal maps and $RMSE$ for the two largest tidal constituents K_1 and M_2 are shown in Fig. 11. Similar spatial distributions for amplitude and phase are observed in both the ROMS and TPXO9 co-tidal maps, however wiggles are present in the phase contours for ROMS. These wiggles are due to internal tides. For both the K_1 and M_2 tidal constituents, we observe the highest $RMSE$s at the southeastern portion of our domain (Fig. 11c, f). While the RMSE for M_2 shows a decreasing trend with increasing distance away from the shoreline, a more complex pattern exists for K_1.

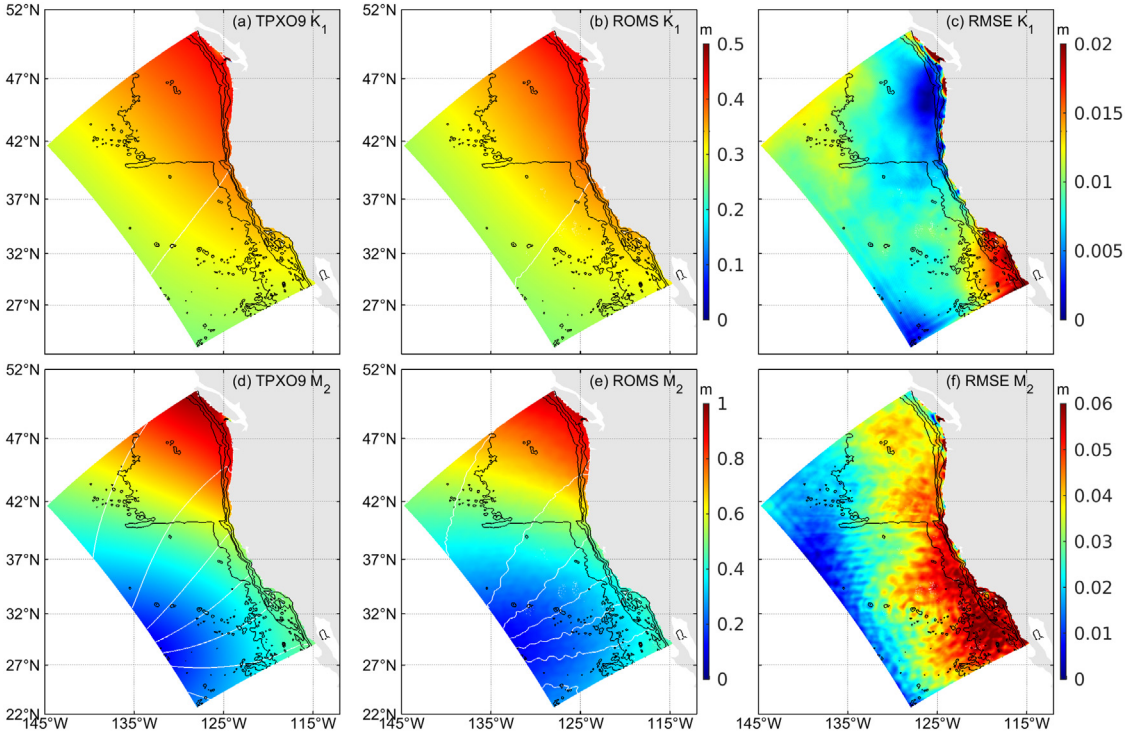

Fig. 11. Barotropic tide validation for K_1 and M_2 tidal constituents. Top panel shows the (a) TPXO9 and (b) ROMS co-tidal plots and (c) RMSE distribution for the K_1 tidal constituent. The bottom row shows the same, but for the M_2 constituent. Thin continuous black lines in (a) to (f) are the same depth contours as in Fig. 1.

Table 2
Baroclinic energy budget of the sponge layers. The flux terms are defined in Fig. 3. The range in $\langle F_r \rangle$ is determined according to the 4 assumptions discussed in Section 2.3. The reflection coefficient $\lambda = \frac{\langle F_r \rangle}{\langle F_{in} \rangle}$. $\langle F_r \rangle$ and λ are shown as $\mu \pm SD$, where μ is the mean over the range of $\langle F_{r,1} \rangle$ to $\langle F_{r,4} \rangle$ and corresponding λ values, and SD is the standard deviation.

Simulation	$\langle F_{out} \rangle$ W/m	$\langle F_{in} \rangle$ W/m	$\langle F_{con} \rangle$ W/m	$\langle D \rangle$ W/m	$\langle F_r \rangle$ W/m	λ %
SS100	368.9	217.6	15.7	107.5	122.4 ± 20.7	56.3 ± 9.5
SS200	322.9	203.4	15.4	126.6	79.8 ± 24.1	39.2 ± 11.8
SS400	275.9	193.2	15.9	150.9	36.6 ± 28.6	18.9 ± 14.8
SS600	261.3	171.0	2.2	70.7	32.9 ± 13.4	19.3 ± 7.8
SS800	250.1	169.5	2.3	80.4	23.2 ± 15.2	13.7 ± 9.0
FS600	285.2	205.0	3.1	82.2	58.0 ± 15.6	28.4 ± 7.6
FS800b	258.9	201.4	3.8	104.7	35.2 ± 19.8	17.5 ± 9.9
FO100	397.1	245.2	14.8	125.9	154.2 ± 23.9	62.9 ± 9.8
FO200	352.0	235.5	15.4	147.0	112.3 ± 27.8	47.7 ± 11.8
FO300	316.8	226.5	16.2	161.5	79.1 ± 30.6	34.9 ± 13.5
FO600	302.8	206.6	3.3	87.1	76.3 ± 16.5	37.0 ± 8.0

Table 3
$RMSE$ and coefficient of determination (R^2_η) for FS800b for O_1, K_1, N_2, M_2 and S_2 tidal constituents. Harmonic analysis using UTide is carried out for 359 days (08 October, 2011–30 September, 2012).

Tidal constituent	O_1	K_1	N_2	M_2	S_2
$RMSE$ (cm)	0.86	0.91	0.80	3.40	1.59
R^2_η (%)	99.64	99.85	98.82	99.06	97.71

To determine if Specified or Flather OBC is best for barotropic tidal forcing, we compare $RMSE$ and R^2_η values obtained for two-month η time series for SS600 and FS600 (Table 4). Area-averaged $RMSE$ and R^2_η estimates are poorer for SS600 as compared to FS600, in particular for the semidiurnal constituents.

3.4.2. Model validation using moorings

We present the variance ratio γ between the simulations and the observations for the velocity variance in three frequency bands for the

Table 4
$RMSE$ and coefficient of determination (R^2_η) for SS600 and FS600 for the O_1, K_1, N_2, M_2 and S_2 tidal constituents. Note that we only consider 01 July to 31 August, 2012 for this analysis.

Tidal constituent	SS600		FS600	
	RMSE (cm)	R^2_η (%)	RMSE (cm)	R^2_η (%)
O_1	3.19	94.26	3.04	95.06
K_1	5.69	93.34	5.32	94.57
N_2	3.39	73.54	3.44	74.50
M_2	16.75	71.22	16.52	74.42
S_2	4.18	80.00	3.75	88.15

HYCOM simulation and ROMS simulations without (FS800a) and with (FS800b) remote internal wave forcing in Table 5 and Fig. 12. Across all frequency bands, FS800a and FS800b have higher γ estimates compared to HYCOM because the higher horizontal and vertical resolution in ROMS allows for an improved generation and resolution of smaller scale internal wave and eddy features. For both HYCOM and ROMS, the super-tidal band has the smallest γ estimates while the semidiurnal band has the highest γ estimates. With remote internal wave forcing (FS800b), the velocity variance is larger than without remote internal wave forcing (FS800a). Because internal tides from Hawaii make up most of the remote semidiurnal internal tides in our domain, it is not surprising that the velocity variance for the semidiurnal band increases in FS800b. The largest increase in velocity variance is for the super-tidal band with $\gamma_{FS800b}/\gamma_{FS800a} = 1.8$.

With remote internal wave forcing, the correlation r between ROMS and observations for the velocity variance increases (Table 5). However, ROMS has poorer correlation with the observations than HYCOM for the semidiurnal band. The smaller correlation in ROMS is attributed to a set of mooring measurements located on top of one of the Spiess seamount chain (127.8100°E, 32.4790°N). The correlation estimate for ROMS for the semidiurnal band improves greatly after removing these outlying mooring data. In addition, the ROMS and HYCOM velocity variances also move closer to the observed variance.

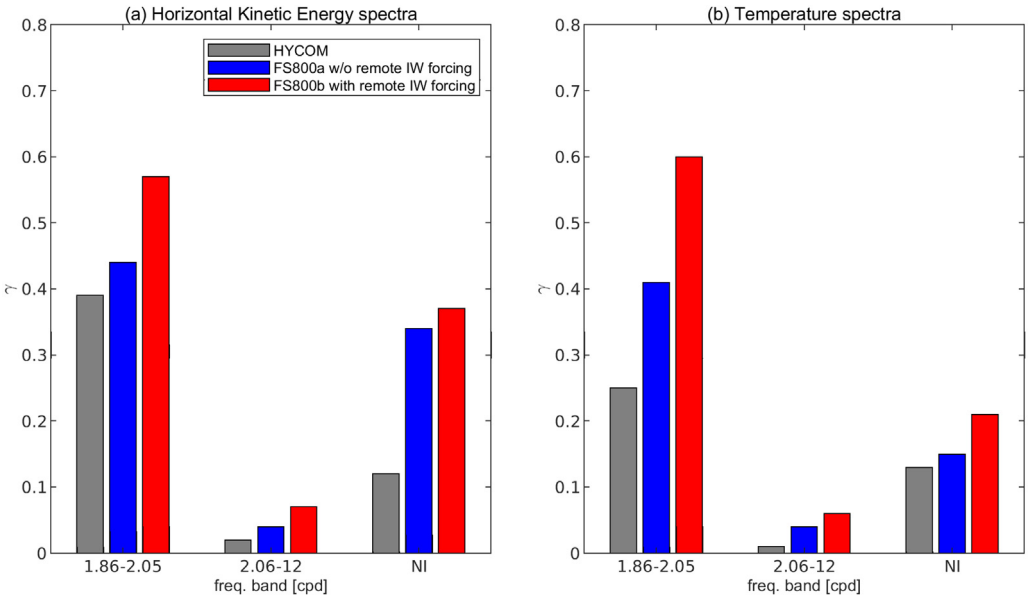

Fig. 12. Ratio of mean modeled variance to mean mooring data variance γ, for (a) the HKE spectra and (b) the temperature spectra for HYCOM and the ROMS simulations without (FS800a) and with (FS800b) remote internal wave forcing for three frequency bands.

Table 5
Velocity variance comparison between moorings and the HYCOM, FS800a, and FS800b simulations. γ and r estimates are compared for three frequency bands. Statistics after removing outliers are in parentheses.

Frequency Band	HYCOM		FS800a		FS800b	
	γ	r	γ	r	γ	r
Semidiurnal: 1.86 – 2.05 cpd	0.39 (0.50)	0.63 (0.59)	0.44 (0.66)	0.10 (0.63)	0.57 (0.85)	0.22 (0.72)
Super-tidal: 2.06 – 12 cpd	0.02 (0.02)	0.72 (0.88)	0.04 (0.05)	0.87 (0.89)	0.07 (0.09)	0.86 (0.91)
Near-inertial: $0.9f$ – 1.74 cpd	0.12 (0.31)	0.55 (0.77)	0.34 (0.44)	0.85 (0.70)	0.37 (0.53)	0.86 (0.74)

Table 6
The same as Table 5 but for the temperature variance. No outliers are present for the temperature variance.

Frequency Band	HYCOM		FS800a		FS800b	
	γ	r	γ	r	γ	r
Semidiurnal: 1.86 – 2.05 cpd	0.25	0.89	0.41	0.92	0.60	0.92
Super-tidal: 2.06 – 12 cpd	0.01	0.92	0.04	0.96	0.06	0.96
Near-inertial: $0.9f$ – 1.74 cpd	0.13	0.92	0.15	0.93	0.21	0.94

Table 7
Root mean square amplitudes ($RMSA$s) for the M_2 baroclinic sea surface height for altimetry and ROMS simulations without (FS800a) and with (FS800b) remote internal wave forcing. FS800a/b are corrected with the stationary variance correction factor as discussed in Section 2.4.3. r is computed after the application of the variance correction factor.

Simulation	$RMSA$ (cm)		r
	Before correction	After correction	
FS800a	0.30	0.28	0.83
FS800b	0.40	0.36	0.98
Altimetry		0.37	

Similar to the velocity variance, γ statistics for the HYCOM simulation are the poorest over all frequency bands for the temperature variance (Table 6, Fig. 12). We record improvements in γ across all frequency bands in FS800b with the presence of remote internal wave forcing. γ is highest for the semidiurnal band ($\gamma = 0.60$). Although we obtain the highest correlation between model and moorings for the super-tidal band, the super-tidal band has the smallest γ estimates. We attribute this to the coarse resolution in our simulations (Luecke et al., 2020), which does not resolve the wave–wave interactions required to obtain the observed high-frequency variance. We anticipate that as we nest down to finer resolutions, γ will improve for the super-tidal band.

3.4.3. Simulated M_2 internal tide validation using altimetry

Finally, we compare the M_2 internal tide η amplitudes for ROMS simulations without (FS800a) and with (FS800b) remote internal wave forcing with the M_2 internal tide η amplitudes inferred from altimetry. Along-track M_2 internal tide amplitudes for altimetry, FS800a and FS800b are shown in Fig. 13a, b and c. The internal tide signals are stronger in the center of the domain. The Mendocino Escarpment and seamounts such as the Spiess seamount chain (Fig. 1) are likely responsible for these strong signals. With the inclusion of remote internal wave forcing, the along-track amplitudes increase almost everywhere in our domain (Fig. 13d and e). The ratio between ROMS and altimetry becomes closer and larger than unity.

The $RMSA$s, before and after the stationary variance corrections (see Section 2.4.3), for FS800a and FS800b, and the RMSA for altimetry are listed in Table 7. $RMSA$s for FS800a and FS800b are 0.30 and 0.40 cm, respectively, before correction. After correction, the $RMSA$s for FS800a and FS800b are 0.28 and 0.36 cm, respectively. The $RMSA$ for the altimetry is 0.37 cm. With remote internal wave forcing at the open boundaries, the $RMSA$ improves by 28% $\left(\frac{0.36-0.28}{0.28}\right)$, but is still 3% smaller than the RMSA of the altimetry data. The ROMS spatial correlation r with altimetry also improves with remote internal wave forcing (Table 7). The along-track spatial correlation increases from 0.83 to 0.98 in the presence of remote internal tides.

In summary, both mooring and altimetry validations show that with remote internal wave forcing, model-data comparison statistics in the regional model simulations improve.

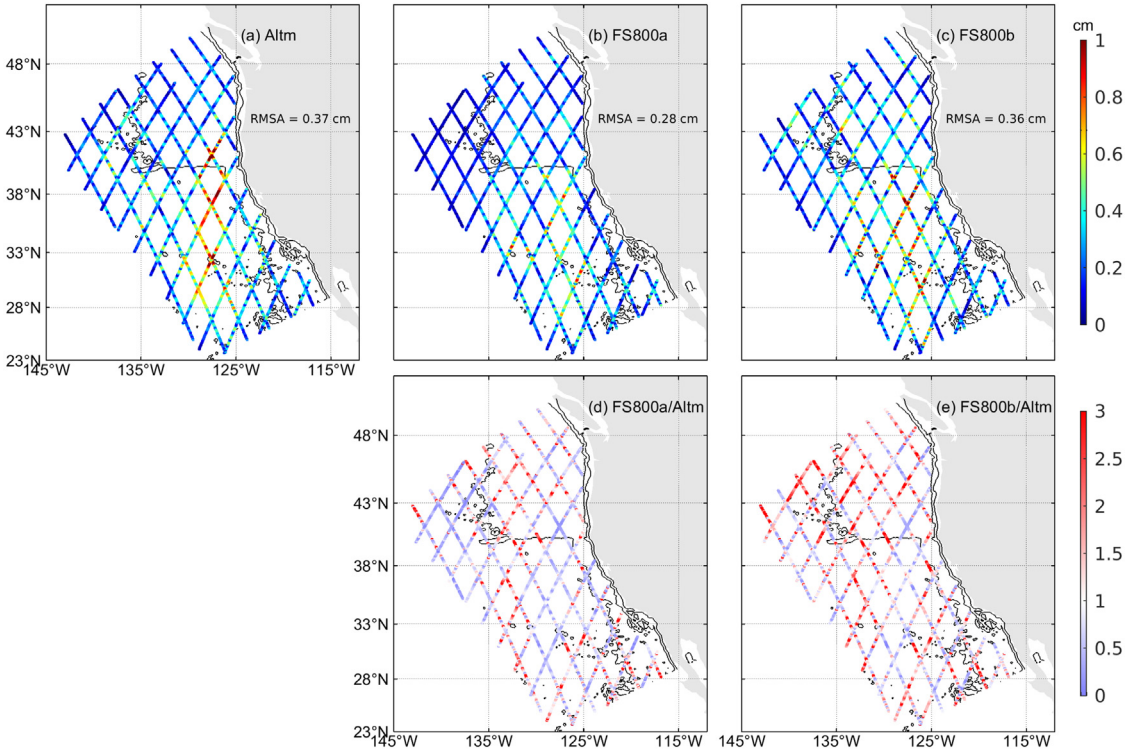

Fig. 13. Along-track M_2 baroclinic η amplitudes for (a) Altimetry, (b) a ROMS simulation with no remote internal wave forcing (FS800a), (c) a ROMS simulation with remote internal wave forcing (FS800b), and ROMS-to-Altimetry amplitude ratios for (d) FS800a and (e) FS800b. Equilibrium correction factors of Buijsman et al. (2020) are applied to ROMS η amplitudes to account for non-stationary effects. Thin continuous black lines in (a) to (c) are the same depth contours as in Fig. 1.

4. Discussion

While we also demonstrate improvement in model-data comparison with the presence of remote internal wave forcing at the open boundaries, this study serves as a precautionary tale for future studies that will consider remote internal wave forcing of regional simulations. We show that the reflections of internal waves generated from the interior can lead to energy buildup and, hence, an apparent improvement of internal wave energetics. As much as 178.9 W/m (λ = 73%) of internal tidal energy generated in the interior gets reflected at the open boundaries for FO100, a simulation with low viscosity values in the sponge layer. We expect internal tide reflections to become worse in regions with a strong outgoing flux and without proper damping at the open boundaries in one-way nested solutions. Of the three open boundaries, only the southern boundary features net outgoing fluxes. This boundary also has the worst reflections. This may be attributed to the finer grid resolution in ROMS that allows internal tidal motions to be better resolved in the CCS than in HYCOM from which we are nesting. One way to mitigate reflections is by adopting sponge layers at the open boundaries. These buffers are expected to absorb internal waves generated from the interior but will also dampen ingoing internal wave fluxes at the open boundaries to some extent. A solution would be to turn on the sponge layers during outgoing flow conditions only. Alternatively, it may be useful to consider two-way nesting for parent and child simulations with the same model (e.g., Debreu and Blayo, 2008; Debreu et al., 2012) to help reduce parent–child grid mismatches at the open boundaries.

The application of Flather or Specified OBC for the barotropic tidal forcing affects the surface tide amplitude and phase, and the barotropic to baroclinic tide conversion in the domain. The agreement with TPXO in the USWC is less when we impose barotropic velocities and sea surface height from HYCOM as hard constraints (i.e., Specified OBCs) at the open boundaries. Unlike the Flather OBC which allows for the mismatch between the interior and exterior solutions to radiate out of the domain, the poor performance of Specified OBC is due to the lack of volume conservation and the presence of reflections at the open boundaries when we clamp the depth-averaged currents and sea surface height (Chapman, 1985; Marchesiello et al., 2001; Mason et al., 2010). This causes a reduction in the surface tide amplitude ($\lesssim$ 10.2%) and in the barotropic-to-baroclinic tide conversion rates ($\lesssim$ 33.3%) for the SS simulations compared to the other simulations with Flather OBC (Table 1).

For the one-year simulations, we capture about 99% of the sea surface elevation variance of TPXO for the O_1, K_1, N_2, M_2 and S_2 tidal constituents. This confirms that the barotropic tides in the east Pacific in HYCOM are well predicted (Arbic et al., 2010; Buijsman et al., 2015, 2020; Ngodock et al., 2016) and the Flather OBC does a good job in propagating external barotropic tidal information. While our model predictions for the barotropic tides are close to those of TPXO, some differences are observed (Fig. 11). Errors in the barotropic tidal predictions could be the result of errors inherited from the parent HYCOM tidal solution. The largest errors in our simulations occur in areas with complex topography such as the southeastern region and the shallow coastal shelf areas (see Fig. 11c, f). These errors may be attributed to the relatively coarse grid and low bathymetry resolution, as well as the omission of coastal estuaries and tidal straits (Wang et al., 2006; Jeon et al., 2019; Zaron and Elipot, 2021). Small scale perturbations to amplitudes and phases are also observed (e.g., in Fig. 11e). Unlike TPXO which is strictly a barotropic tidal model, our ROMS simulations allow for the generation of internal tides. The stripy patterns at the southernmost corner of the domain in Fig. 11c and the westernmost corner in Fig. 11f are due to reflected internal tide signals. The distance between the stripes is ~80 km, which is half the wavelength of a mode one M_2 internal tide near the USWC. This is in agreement with a standing wave pattern in which antinodes (nodes) are separated by half wavelength. Finally, Janekovic and Powell (2012) showed that tidal errors increase for lower boundary forcing frequencies. However, the 1 cycle per hour barotropic forcing frequency that is used in this study does not cause significant errors according to Figure A2 of Janekovic and Powell (2012).

While the ROMS simulations use finer horizontal and vertical resolutions compared to the parent HYCOM solution, the ROMS simulations have less agreement with the moorings on top of one of the Spiess seamount chain (127.8100°E, 32.4790°N) as compared to the HYCOM simulation. Although the vertical profiles of semidiurnal horizontal kinetic energy in HYCOM and ROMS have the same spatial patterns, these patterns are offset at the mooring depths (453–629 m; results not shown). This offset is due to the differences in the stratification profiles over this seamount in the ROMS and HYCOM simulations. The different stratification profiles cause different eigenfunction shapes of the internal wave modes, causing different vertical internal tide kinetic energy distributions.

In addition to loosing energy due to topographic scattering and nonlinear wave–wave interactions (Kelly et al., 2012, 2013; Olbers et al., 2020), low mode internal tides are likely to become non-phase-locked when they interact with time varying stratification, mean background currents, and vorticity along their propagation paths (Rainville and Pinkel, 2006; Zaron and Egbert, 2014; Buijsman et al., 2017; Kumar et al., 2019). While forcing regional models with phase-locked internal tides, e.g., from HRET (Zaron, 2019; Gong et al., 2021), may be sufficient for domains close to internal tide generation sites, it may be insufficient for model domains located thousands of km from generation sites. At the USWC, phase-locked internal tides extracted from a one year simulation contribute only 34% of the total semidiurnal baroclinic flux into the domain. Hence, such forcing would underestimate the internal tide energy in the domain.

In addition, NIWs may be an important fraction of high-frequency baroclinic forcing of regional simulations. For instance, NIWs contribute more than half of the high-frequency baroclinic fluxes at our domain's northern and southern boundaries (Fig. 5). Hence, depending on the region of interest, it may be important to include non-phase-locked internal tides and NIWs when considering high-frequency baroclinic forcing of regional simulations.

To conclude our discussion, we note that the performance of the remote internal waves in the regional simulation also depends on which global model simulation is used for the remote forcing. For instance, Buijsman et al. (2020) obtained a 34% increase in mode-1 M_2 internal tide energy for their 4-km horizontal resolution global HYCOM simulation (H25) compared to the 8-km expt_06.1 simulation we use in this study. They also observed better agreement to observations for the H25 simulation. They attributed the increase in internal tide energy in H25 to increased topographic conversion and reduced wave-drag strength. Hence, it is possible that the model-data comparison statistics reported in this study would improve if we were to force our model with the high-frequency fields from H25. However, we do not have a 1 year simulation of H25 at our disposal.

5. Summary and conclusions

In this study, in addition to astronomical tidal forcing, we force realistic regional ROMS simulations of the U.S. West Coast with subtidal fields from a basin scale ROMS simulation, and with surface tides and remote internal waves from a global ocean HYCOM simulation with realistic tidal and atmospheric forcing. The global model includes remotely generated internal tides and near-inertial waves that propagate over long distances. We test Specified and Flather open boundary conditions (OBCs) for the barotropic mode, and Specified and modified Orlanski OBCs for the baroclinic mode. To control the reflections of internal waves from the interior of the domain, we add sponge layers of varying width and viscosities at the open boundaries. We quantify internal tide reflections at the open boundaries using a Discrete Fourier Transform (DFT) technique in combination with an internal wave energy budget for the sponge layer. Lastly, we compare simulations with minimum internal tide reflections against observations.

Simulated barotropic tide amplitudes and phases are closer to those of TPXO9-atlas when Flather instead of Specified OBC is used for barotropic tides. We also find that the modified Orlanski OBC is less efficient in handling dispersive outgoing internal waves as compared to the Specified OBC. Furthermore, our reflection analysis reveals a decrease in internal tide reflections at the open boundaries with an increase in sponge viscosity and/or sponge width. We find that the Flather–Specified barotropic–baroclinic OBC combination with a 58 km wide sponge layer with a maximum viscosity of 800 m^2/s is the most optimal open boundary setup for remote internal wave forcing. This setup yields a reflection coefficient $\lambda = 17.5 \pm 9.9\%$.

Asides from the OBC sensitivity tests, we report improvements in model-data comparisons with the presence of remote internal wave forcing at the open boundaries. With remote high-frequency baroclinic forcing, the simulated variance in velocity and temperature increases for the tidal, near-inertial and super-tidal frequency bands, and approaches the variance in the mooring data. Moreover, the correlations also improve. While the 4-km horizontal resolution adopted in this study does a relatively good job in resolving mesoscale, near-inertial and tidal motions, super-tidal motions are still poorly resolved. Hence, the lowest simulated variance as a fraction of the observed variance (γ) is observed in the super-tidal frequency band. The semidiurnal band variance in the simulation with remote internal wave forcing is closest to observations. Also, about 97% ($\frac{0.36cm}{0.37cm}$) of altimetry M_2 internal tide sea surface height root mean square amplitude ($RMSA$) is captured in the simulation with remote internal wave forcing. Finally, along-track correlation with altimetry increases from 0.83 to 0.98 when remote internal wave forcing is included.

In accordance with Nelson et al. (2020) and Mazloff et al. (2020), this study confirms that the model-data agreement improves when remote internal wave forcing is included. Hence, it may be important for future regional ocean simulation studies to consider adding realistic high-frequency baroclinic forcing at the open boundaries. However, these studies should also consider implementing the best open boundary conditions to minimize excessive reflections of internal waves from the interior, which may incorrectly increase internal wave energy levels.

CRediT authorship contribution statement

Oladeji Q. Siyanbola: Conceptualization, Formal analysis, Visualization, Writing – original draft, Writing – review & editing. **Maarten C. Buijsman:** Conceptualization, Formal analysis, Funding acquisition, Project administration, Visualization, Writing – original draft, Writing – review & editing. **Audrey Delpech:** Software, Writing – review & editing. **Lionel Renault:** Resources, Software, Writing – review & editing. **Roy Barkan:** Resources, Software, Funding acquisition, Writing – review & editing. **Jay F. Shriver:** Resources, Software. **Brian K. Arbic:** Resources, Funding acquisition, Writing – review & editing. **James C. McWilliams:** Resources, Software, Funding acquisition.

Declaration of competing interest

The authors declare that they have no known competing financial interests or personal relationships that could have appeared to influence the work reported in this paper.

Data availability

We have provided weblinks to datasets and codes used in this study in the Acknowledgments section.

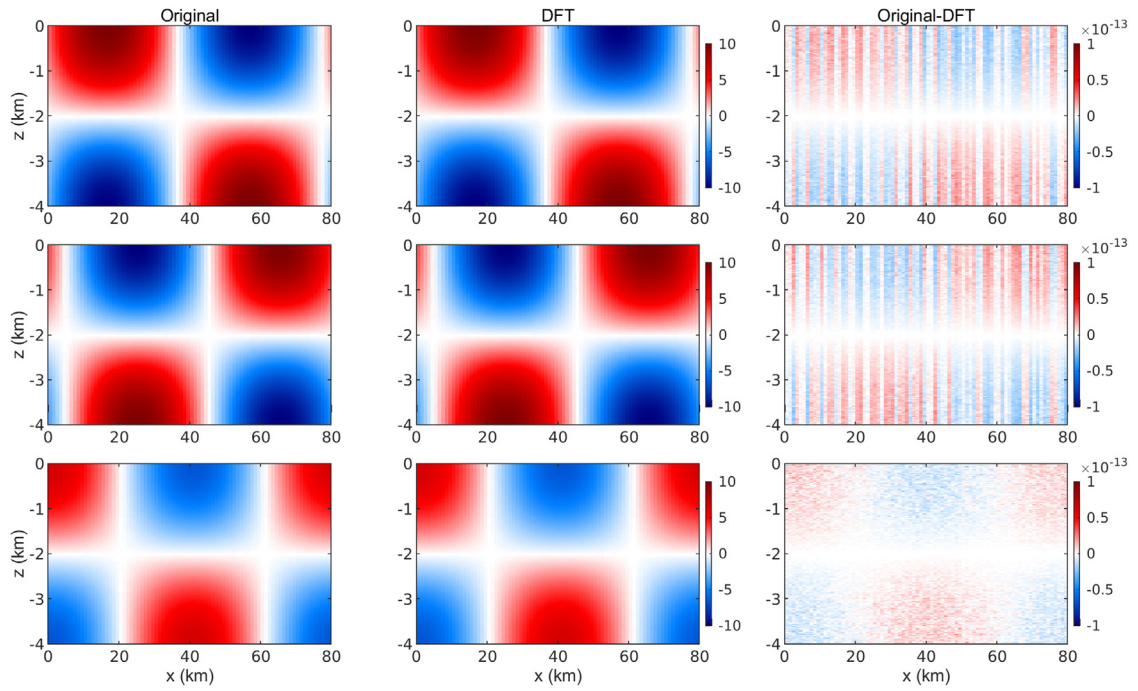

Fig. A.14. The application of the DFT technique to a standing mode 1 wave in an idealized ocean with uniform stratification (N = 1 x 10^{-3} rad/s). All images are snapshots at t = 50 h. First row shows rightward propagating mode 1 waves, second row is for leftward propagating mode 1 waves, and the bottom row is for the resulting standing waves (leftward + rightward). First column shows the original vertical structure, the second column shows the filtered components, and the last column shows the difference between the original and filtered waves.

Acknowledgments

O.Q. Siyanbola and M.C. Buijsman are funded by the National Science Foundation (NSF), USA grant OCE1851397. A. Delpech, R. Barkan and J.C. McWilliams receive funding from NSF, USA grant OCE1851376. R. Barkan is also supported by the Israeli Science Foundation grant 1736/18. L. Renault receives funding from CNES project I-CASCADE and CARAMBA. J.F. Shriver is supported by ONR Task Force Ocean grant N0001422WX00941. B.K. Arbic acknowledges support from NSF grant OCE1851164. We thank the anonymous reviewers for their constructive comments which were helpful improving the manuscript.

The TPXO9 data used was obtained from https://www.tpxo.net/global/tpxo9-atlas. The GMACMD moored historical observations were downloaded from the University of Michigan Library archival system (https://doi.org/10.7302/dbfp-s644). The CCE mooring data were collected and made available by the Scripps Institution of Oceanography (http://mooring.ucsd.edu/cce/index.php). Altimeter dataset used for validation purposes and samples of our model output can be accessed online (https://doi.org/10.5281/zenodo.7194957). The MATLAB DFT and the HYCOM to ROMS interpolation scripts used in this study are available from the GitHub repositories https://github.com/Oladeji17/matlab/tree/main/DFT and https://github.com/Oladeji17/matlab/tree/main/H2R, respectively.

Appendix. Unidirectional separation technique

At the open boundaries, we separate baroclinic fluxes into ingoing and outgoing components using the Discrete Fourier Transform (DFT) technique. We follow similar steps to those outlined in section 2.1 of Gong et al. (2021).

In this appendix, we demonstrate how effective the DFT technique is when applied to an analytical standing wave, comprising leftward and rightward propagating mode 1 sinusoidal waves. We use the DFT technique to separate the leftward and rightward components of our standing wave. The length of our time series is 60 M_2 tidal cycles. For this analysis, the Brünt-Vä isälä frequency N, the Coriolis frequency f, and the water depth h are similar to those used on page 76 of Gerkema and Zimmerman (2008). Our mode 1 waves are generated using Equation (5.23) of Gerkema and Zimmerman (2008). Time snapshots of the results are shown in Fig. A.14. The difference between the separated fields obtained using the DFT technique and the original wave signals are very small.

We also demonstrate that the DFT separation technique is accurate when applied to a complex wave field. The ingoing and outgoing flux vectors at the open boundaries of our regional domain obtained with the DFT code for the global HYCOM simulation are shown in Fig. A.15. The internal tide beams in Fig. 5a are well represented by the DFT technique, e.g., beams at 36°N at the western boundary and 42°N at the northern boundary. The boundaries that act as sources of internal tide energy (west and north) feature ingoing fluxes that are larger than the outgoing fluxes. In contrast, outgoing fluxes are larger than the ingoing fluxes at the southern boundary. As a check, we compare the net fluxes using the DFT technique (ingoing + outgoing + cross terms) with the undecomposed fluxes and find them to be equal (Table A.8).

Because our decomposition technique is based on the DFT, amplitude and phase errors will be present at the tails when the original signal is not periodic in space. This is expected to happen when applying the DFT technique to realistic simulations. We illustrate this phenomenon by considering the superposition of two non-periodic signals propagating in opposite directions (Fig. A.16). Although, there is a good agreement between the DFT and the original standing wave signals, the leftward and rightward constituents from the DFT technique are not in good agreement with those of the original signals at the tail ends. This is reflected in the decreasing R^2 values near the tail ends (Fig. A.16). We obtain spurious fluxes at the tail ends of our chosen transects when we apply the DFT code. However, the sponge interior edges along which we obtain our estimates for F_{in} and F_{out} are farther away from the tail ends where amplitude and phase errors are likely to be significant. Lastly, the lengths of the transects that are perpendicular to the boundary should be chosen such that they are not smaller than the wavelength of a mode 1 internal wave in the region of consideration.

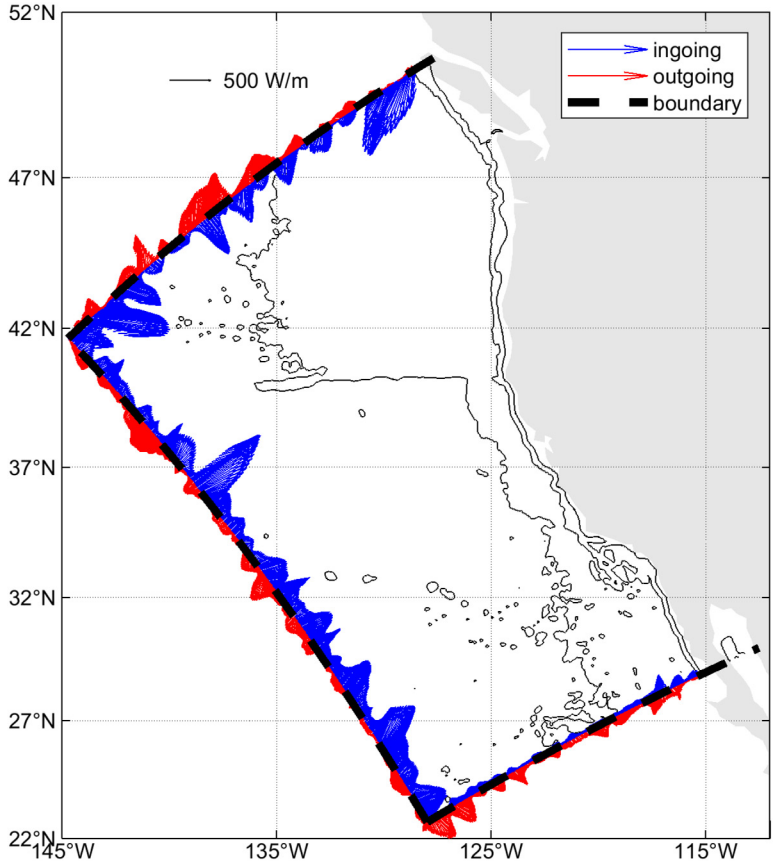

Fig. A.15. Depth-integrated and time-mean (01 July–31 August, 2012) semidiurnal unidirectional ingoing and outgoing HYCOM fluxes at the open boundaries of the computational domain. The regional simulations are forced at the open boundaries with the total HYCOM high-frequency fields and not with the unidirectional fields. Thin continuous black lines are the same depth contours as in Fig. 1.

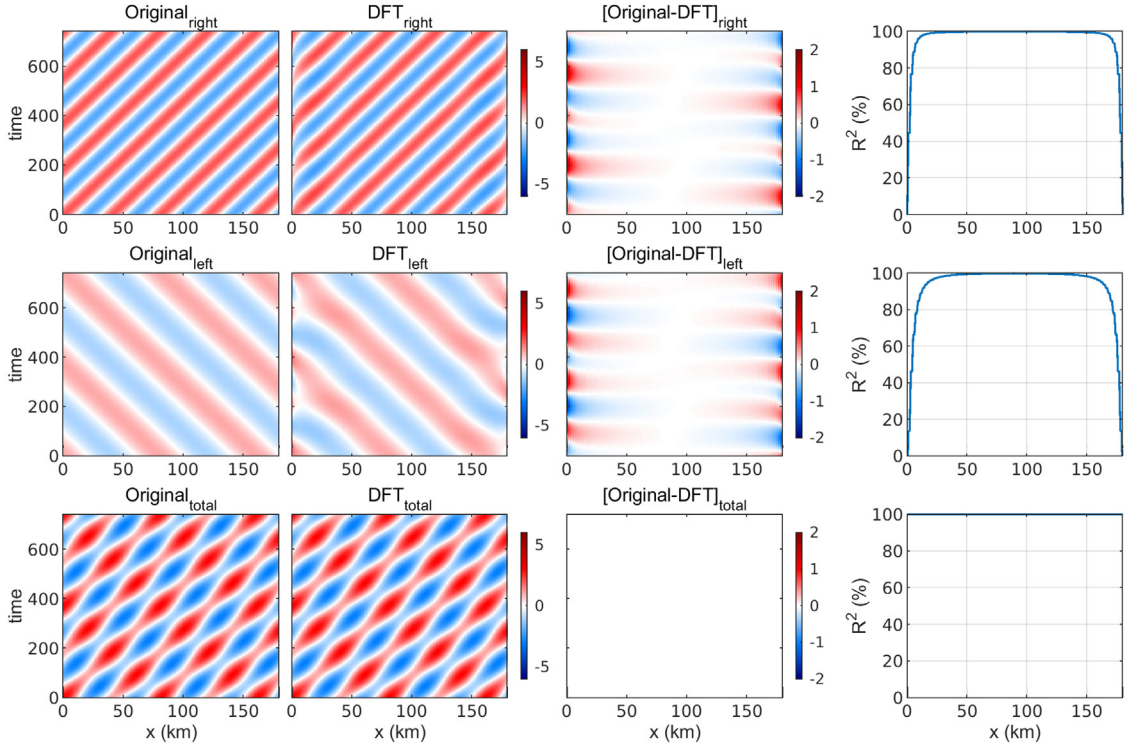

Fig. A.16. Decomposition of non-periodic analytical standing wave signals. First column is for the original rightward, leftward and resulting standing wave (leftward + rightward), the second column is for those obtained using the DFT technique, the third column is for the difference between the original and the filtered waves, and the last column shows the coefficient of determination (R^2).

Table A.8
Depth-integrated and time-mean (01 July–31 August, 2012) semidiurnal ingoing, outgoing and cross-term fluxes from HYCOM for the western, northern and southern boundaries. Values in W/m are in parentheses.

Boundary	Ingoing MW (W/m)	Outgoing MW (W/m)	Cross terms MW (W/m)	$\Sigma\langle F_{\mathrm{DFT}}\rangle$ MW (W/m)	$\Sigma\langle F_{\mathrm{undecomposed}}\rangle$ MW (W/m)
West	854.9 (323.3)	−269.8 (−102.0)	1.4 (0.5)	586.5 (221.8)	586.5 (221.8)
North	331.9 (205.9)	−174.5 (−108.2)	16.7 (10.4)	174.1 (108.1)	174.1 (108.1)
South	144.2 (95.9)	−218.1 (−145.0)	−4.1 (−2.7)	−77.9 (−51.8)	−77.9 (−51.8)

References

Ansong, J.K., Arbic, B.K., Buijsman, M.C., Richman, J.G., Shriver, J.F., Wallcraft, A.J., 2015. Indirect evidence for substantial damping of low-mode internal tides in the open ocean. J. Geophys. Res. 120, 6057–6071. http://dx.doi.org/10.1002/2015JC010998.

Arbic, B.K., Alford, M.H., Ansong, J.K., Buijsman, M.C., Ciotti, R.B., Farrar, J.T., Hallberg, R.W., Henze, C.E., Hill, C.N., Luecke, C.A., Menemenlis, D., Metzger, E.J., Müller, M., Nelson, A.D., Nelson, B.C., Ngodock, H.E., Ponte, R.M., Richman, J.G., Savage, A.C., Scott, R.B., Shriver, J.F., Simmons, H.L., Souopgui, I., Timko, P.G., Wallcraft, A.J., Zamudio, L., Zhao, Z., 2018. A primer on global internal tide and internal gravity wave continuum modeling in HYCOM and MITgcm. In: Chassignet, E., Pascual, A., Tintoré, J., Verron, J. (Eds.), New Frontiers in Operational Oceanography. GODAE OceanView, pp. 307–392. http://dx.doi.org/10.17125/gov2018.ch13.

Arbic, B.K., Garner, S.T., Hallberg, R.W., Simmons, H.L., 2004. The accuracy of surface elevations in forward global barotropic and baroclinic tide models. Deep-Sea Res. II 51, 3069–3101. http://dx.doi.org/10.1016/j.dsr2.2004.09.014.

Arbic, B.K., Wallcraft, A.J., Metzger, E.J., 2010. Concurrent simulation of the eddying general circulation and tides in a global ocean model. Ocean Model. 32, 175–187. http://dx.doi.org/10.1016/j.ocemod.2010.01.007.

Becker, J.J., Sandwell, D.T., Smith, W.H.F., Braud, J., Binder, B., Depner, J., Fabre, D., Factor, J., Ingalls, S., Kim, S.-H., Ladner, R., Marks, K., Nelson, S., Pharaoh, A., Trimmer, R., Von Rosenberg, J., Wallace, G., Weatherall, P., 2009. Global bathymetry and elevation data at 30 arc seconds resolution: SRTM30_PLUS. Mar. Geod. 32, 355–371. http://dx.doi.org/10.1080/01490410903297766.

Bleck, R., Halliwell, G., Wallcraft, A., Carroll, S., Kelly, K., Rushing, K., 2002. HYbrid coordinate ocean model (HYCOM). User's Manual. p. 211.

Buijsman, M.C., Ansong, J.K., Arbic, B.K., Richman, J.G., Shriver, J.F., Timko, P.G., Wallcraft, A.J., Whalen, C.B., Zhao, Z., 2016. Impact of parameterized internal wave drag on the semidiurnal energy balance in a global ocean circulation model. J. Phys. Oceanogr. 46, 1399–1419. http://dx.doi.org/10.1175/JPO-D-15-0074.1.

Buijsman, M.C., Arbic, B.K., Green, J.A.M., Helber, R.W., Richman, J.G., Shriver, J.F., Timko, P.G., Wallcraft, A., 2015. Optimizing internal wave drag in a forward barotropic model with semidiurnal tides. Ocean Model. 85, 42–55. http://dx.doi.org/10.1016/j.ocemod.2014.11.003.

Buijsman, M.C., Arbic, B.K., Richman, J.G., Shriver, J.F., Wallcraft, A.J., Zamudio, L., 2017. Semidiurnal internal tide incoherence in the equatorial Pacific. J. Geophys. Res. Oceans 122, 5286–5305. http://dx.doi.org/10.1002/2016JC012590.

Buijsman, M.C., McWilliams, J.C., Jackson, C.R., 2010. East–west asymmetry in nonlinear internal waves from Luzon Strait. J. Geophys. Res. 115 (C10057), http://dx.doi.org/10.1029/2009JC006004.

Buijsman, M.C., Stephenson, G.R., Ansong, J.K., Arbic, B.K., Green, J.A.M., Richman, J.G., Shriver, J.F., Vic, C., Wallcraft, A.J., Zhao, Z., 2020. On the interplay between horizontal resolution and wave drag and their effect on tidal baroclinic mode waves in realistic global ocean simulations. Ocean Modell. 152. http://dx.doi.org/10.1016/j.ocemod.2020.101656.

Buijsman, M.C., Uchiyama, Y., McWilliams, J.C., Hill-Lindsay, C.R., 2012. Modeling semidiurnal internal tide variability in the Southern California Bight. J. Phys. Oceanogr. 42, 62–77. http://dx.doi.org/10.1175/2011JPO4597.1.

Carter, G.S., Merrifield, M.A., Becker, J.M., Katsumata, K., Gregg, M.C., Luther, D.S., Levine, M.D., Boyd, T.J., Firing, Y.L., 2008. Energetics of M_2 barotropic to baroclinic tidal conversion at the Hawaiian Islands. J. Phys. Oceanogr. 38, 2205–2223. http://dx.doi.org/10.1175/2008JPO3860.1.

Chapman, D.C., 1985. Numerical treatment of cross-shelf open boundaries in a barotropic coastal ocean model. J. Phys. Oceanogr. 15, 1060–1075.

Chassignet, E.P., Hurlburt, H.E., Smedstad, O.M., Halliwell, G.R., Hogan, P.J., Wallcraft, A.J., Baraille, R., Bleck, R., 2007. The HYCOM (HYbrid Coordinate Ocean Model) data assimilative system. Mar. Syst. 65, 60–83. http://dx.doi.org/10.1016/j.jmarsys.2005.09.016.

Chen, X., Liu, C., O'Driscoll, K., Mayer, B., Su, J., Pohlmann, T., 2013. On the nudging terms at open boundaries in regional ocean models. Ocean Model. 66, 14–25. http://dx.doi.org/10.1016/j.ocemod.2013.02.006.

Codiga, D.L., 2011. Unified Tidal Analysis and Prediction using the UTide Matlab Functions. Technical Report 2011-01, Graduate School of Oceanography, University of Rhode Island, Narragansett, RI, p. 59.

Debreu, L., Blayo, E., 2008. Two-way embedding algorithms: a review. Ocean Dyn. 58, 415–428. http://dx.doi.org/10.1007/s10236-008-0150-9.

Debreu, L., Marchesiello, P., Penven, P., Cambon, G., 2012. Two-way nesting in split-explicit ocean models: Algorithms, Implementation and Validation. Ocean Modell. 49-50, 1–21. http://dx.doi.org/10.1016/j.ocemod.2012.03.003.

Dushaw, B.D., Howe, B.M., Cornuelle, B.D., Worcester, P.F., Luther, D.S., 1995. Barotropic and baroclinic tides in the central north Pacific ocean determined from long-range reciprocal acoustic transmissions. J. Phys. Oceanogr. 25, 631–647.

Egbert, G.D., Bennett, A.F., Foreman, M.G.G., 1994. TOPEX/POSEIDON tides estimated using a global inverse model. J. Geophys. Res. 99, 24821–24852.

Egbert, G.D., Erofeeva, S.Y., 2002. Efficient inverse modeling of barotropic ocean tides. J. Atmos. Ocean. Technol. 19, 183–204.

Egbert, G.D., Ray, R.D., 2000. Significant dissipation of tidal energy in the deep ocean inferred from satellite altimeter data. Nature 405, 775–778. http://dx.doi.org/10.1038/35015531.

Egbert, G.D., Ray, R.D., 2003. Semidiurnal and diurnal tidal dissipation from TOPEX/Poseidon altimetry. Geophys. Res. Lett. 30, http://dx.doi.org/10.1029/2003GL017676.

Flather, R.A., 1976. A tidal model of the northwest European continental shelf. In: Memoirs de la Societe Royale Des Sciences de Liege. Vol. 6. pp. 141–164.

Fu, L.-L., Alsdorf, D., Morrow, R., Rodrigues, E., Mognard, N., 2012. SWOT: The Surface Water and Ocean Topography Mission - Wide-Swath Altimetric Measurement of Water Elevation on Earth. JPL Publication, p. 12.

Garrett, C., Munk, W., 1975. Space–time scales of internal waves: A progress report. J. Geophys. Res. 80, 291–297.

Gerkema, T., Zimmerman, J.T.F., 2008. An Introduction to Internal Waves. In: Lecture Notes, Royal Netherlands Institute for Sea Research.

Gong, Y., Rayson, M.D., Jones, N.L., Ivey, G.N., 2021. Directional decomposition of internal tides propagating from multiple generation sites. Ocean Model. (162), http://dx.doi.org/10.1016/j.ocemod.2021.101801.

Hogan, T.F., Liu, M., Ridout, J.A., Peng, M.S., Whitcomb, T.R., Ruston, B.C., Reynolds, C.A., Eckermann, S.D., Moskaitis, J.R., Baker, N.L., McCormack, J.P., Viner, K.C., McLay, J.G., Flatau, M.K., Xu, L., Chen, C., Chang, S.W., 2014. The navy global environmental model. Oceanography 27, 116–125. http://dx.doi.org/10.5670/oceanog.2014.73.

Janekovic, I., Powell, B., 2012. Analysis of imposing tidal dynamics to nested numerical models. Cont. Shelf Res. 34, 30–40. http://dx.doi.org/10.1016/j.csr.2011.11.017.

Jayne, S.R., St. Laurent, L.C., 2001. Parameterizing tidal dissipation over rough topography. Geophys. Res. Lett. 28, 811–814. http://dx.doi.org/10.1029/2000GL012044.

Jeon, C.-H., Buijsman, M.C., Wallcraft, A.J., Shriver, J.F., Arbic, B.K., Richman, J.G., Hogan, P.J., 2019. Improving surface tidal accuracy through two-way nesting in a global ocean model. Ocean Model. 137, 98–113. http://dx.doi.org/10.1016/j.ocemod.2019.03.007.

Kang, D., Fringer, O., 2012. Energetics of barotropic and baroclinic tides in the Monterey Bay Area. J. Phys. Oceanogr. 42, 272–290. http://dx.doi.org/10.1175/JPO-D-11-039.1.

Kelly, S.M., Jones, N.L., Nash, J.D., Waterhouse, A.F., 2013. The geography of semidiurnal mode-1 internal-tide energy loss. Geophys. Res. Lett. 40, 4689–4693. http://dx.doi.org/10.1002/grl.50872.

Kelly, S.M., Nash, J.D., 2010. Internal-tide generation and destruction by shoaling internal tides. Geophys. Res. Lett. 37 (L23611), http://dx.doi.org/10.1029/2010GL045598.

Kelly, S.M., Nash, J.D., Kunze, E., 2010. Internal-tide energy over topography. Geophys. Res (115), http://dx.doi.org/10.1029/2009JC005618.

Kelly, S.M., Nash, J.D., Martini, K.I., Alford, M.H., Kunze, E., 2012. The cascade of tidal energy from low to high modes on a continental slope. J. Phys. Oceanogr. 42, 1217–1232. http://dx.doi.org/10.1175/JPO-D-11-0231.1.

Kerry, C.G., Powell, B.S., Carter, G.S., 2013. Effects of remote generation sites on model estimates of M_2 internal tides in the Philippine sea. J. Phys. Oceanogr. 43, 187–204. http://dx.doi.org/10.1175/JPO-D-12-081.1.

Kumar, N., Suanda, S.H., Colosi, J.A., Hass, K., Di Lorenzo, E., Miller, A.J., Edwards, C.A., 2019. Coastal semidiurnal internal tidal incoherence in the Santa Maria Basin, California: Observations and model simulations. J. Geophys. Res. Oceans 124, 5158–5179. http://dx.doi.org/10.1029/2018JC014891.

Kunze, E., Rosenfeld, L.K., Carter, G.S., Gregg, M.C., 2002. Internal waves in Monterey Submarine Canyon. J. Phys. Oceanogr. 32, 1890–1913.

Large, W.B., 2006. Surface fluxes for practitioners of global ocean data assimilation. In: Chassignet, E.P., Verron, J. (Eds.), Ocean Weather Forecasting. Springer, pp. 229–270. http://dx.doi.org/10.1007/1-4020-4028-8_9.

Li, Q., Farmer, D.M., Duda, T.F., Ramp, S., 2009. Acoustical measurements of nonlinear internal waves using the inverted echo sounder. Atmos. Ocean. Technol. 26, 2228–2242. http://dx.doi.org/10.1175/2009JTECHO652.1.

Luecke, C.A., Arbic, B.K., Richman, J.G., Shriver, J.F., Alford, M.H., Ansong, J.K., Bassette, S.L., Buijsman, M.C., Menemenlis, D., Scott, R.B., Timko, P.G., Voet, G., Wallcraft, A.J., Zamudio, L., 2020. Statistical comparisons of temperature variance and kinetic energy in global ocean models and observations: Results from mesoscale to internal wave frequencies. J. Geophys. Res. Oceans 125, http://dx.doi.org/10.1029/2019JC015306, e2019JC015306.

Marchesiello, P., McWilliams, J.C., Shchepetkin, A., 2001. Open boundary conditions for long-term integration of regional oceanic models. Ocean Modell. 3, 1–20. http://dx.doi.org/10.1016/S1463-5003(00)00013-5.

Mason, E., Molemaker, J., Shchepetkin, A.F., Colas, F., McWilliams, J.C., Sangrà, P., 2010. Procedures for offline grid nesting in regional ocean models. Ocean Model. 35, 1–15. http://dx.doi.org/10.1016/j.ocemod.2010.05.007.

Mazloff, M.R., Cornuelle, B., Gille, S.T., Wang, J., 2020. The importance of remote forcing for regional modeling of internal waves. J. Geophys. Res. 125, http://dx.doi.org/10.1029/2019JC015623, e2019JC015623.

Munk, W., Wunsch, C., 1998. Abyssal recipes II: energetics of tidal and wind mixing. Deep-Sea Res. I 45, 1977–2010. http://dx.doi.org/10.1016/S0967-0637(98)00070-3.

Nash, J.D., Alford, M.H., Kunze, E., 2005. Estimating internal wave energy fluxes in the ocean. Atmos. Ocean. Technol. 22, 1551–1570. http://dx.doi.org/10.1175/JTECH1784.1.

Nelson, A.D., Arbic, B.K., Menemenlis, D., Peltier, W.R., Alford, M.H., Grisouard, N., Klymak, J.M., 2020. Improved internal wave spectral continuum in a regional ocean model. J. Geophys. Res. 125, http://dx.doi.org/10.1029/2019JC015974.

Ngodock, H.E., Souopgui, I., Wallcraft, A.J., Richman, J.G., Shriver, J.F., Arbic, B.K., 2016. On improving the accuracy of the M_2 barotropic tides embedded in a high-resolution global ocean circulation model. Ocean Model. 97, 16–26. http://dx.doi.org/10.1016/j.ocemod.2015.10.011.

Nycander, J., Doos, K., 2003. Open boundary conditions for barotropic waves. J. Geophys. Res. 108, http://dx.doi.org/10.1029/2002JC001529.

Ohman, M.D., Rudnick, D.L., Chekalyuk, A., Davis, R.E., Feely, R.A., Kahru, M., Kim, H.-J., Landry, M.R., Martz, T.R., Sabine, C.L., Send, U., 2013. Autonomous ocean measurements in the California Current Ecosystem. Oceanography 26, 18–25. http://dx.doi.org/10.5670/oceanog.2013.41.

Olbers, D., Pollmann, F., Eden, C., 2020. On PSI interactions in internal gravity wave fields and the decay of baroclinic tides. J. Phys. Oceanogr. 50, 751–771. http://dx.doi.org/10.1175/JPO-D-19-0224.1.

Orlanski, I., 1976. A simple boundary condition for unbounded hyperbolic flows. J. Comput. Phys. 21, 251–269. http://dx.doi.org/10.1016/0021-9991(76)90023-1.

Palma, E.D., Matano, R.P., 1998. On the implementation of passive open boundary conditions for a general circulation model: The barotropic mode. J. Geophys. Res. 103, 1319–1341. http://dx.doi.org/10.1029/97JC02721.

Rainville, L., Pinkel, R., 2006. Propagation of low-mode internal waves through the ocean. J. Phys. Oceanogr. 36, 1220–1236. http://dx.doi.org/10.1175/JPO2889.1.

Raja, K.J., Buijsman, M.C., Shriver, J.F., Arbic, B.K., Siyanbola, O., 2022. Near-inertial wave energetics modulated by background flows in a global model simulation. J. Phys. Oceanogr. 52, 823–840. http://dx.doi.org/10.1175/JPO-D-21-0130.1.

Ray, R.D., Zaron, E.D., 2011. Non-stationary internal tides observed with satellite altimetry. Geophys. Res. Lett. 38 (L17609), http://dx.doi.org/10.1029/2011GL048617.

Ray, R.D., Zaron, E.D., 2016. M_2 internal tides and their observed wavenumber spectra from satellite altimetry. J. Phys. Oceanogr. 46, 3–22. http://dx.doi.org/10.1175/JPO-D-15-0065.1.

Renault, L., Hall, A., McWilliams, J.C., 2016. Orographic shaping of US West Coast wind profiles during the upwelling season. Clim. Dynam. 46, 273–289. http://dx.doi.org/10.1007/s00382-015-2583-4.

Renault, L., Masson, S., Arsouze, T., Madec, G., McWilliams, J.C., 2020. Recipes for how to force oceanic model dynamics. In: Advances in Modeling Earth Systems. Vol. 12. http://dx.doi.org/10.1029/2019MS001715.

Renault, L., McWilliams, J.C., Kessouri, F., Jousse, A., Frenzel, H., Chen, R., Deutsch, C., 2021. Evaluation of high-resolution atmospheric and oceanic simulations of the California Current System. Prog. Oceanogr. (195), http://dx.doi.org/10.1016/j.pocean.2021.102564.

Rocha, C.B., Gille, S.T., Chereskin, T.K., Menemenlis, D., 2016. Seasonality of submesoscale dynamics in the Kuroshio Extension. J. Geophys. Res. Lett. 43, 11304–11311. http://dx.doi.org/10.1002/2016GL071349.

Scott, R.B., Arbic, B.K., Chassignet, E.P., Coward, A.C., Maltrud, M., Merryfield, W.J., Srinivasan, A., Varghese, A., 2010. Total kinetic energy in four global eddying ocean circulation models and over 5000 current meter records. Ocean Model. 32, 157–169. http://dx.doi.org/10.1016/j.ocemod.2010.01.005.

Shchepetkin, A.F., McWilliams, J.C., 2005. The regional oceanic modeling system (ROMS): a split-explicit, free-surface, topography-following-coordinate oeanic model. Ocean Modell. 9, 347–404. http://dx.doi.org/10.1016/j.ocemod.2004.08.002.

Shchepetkin, A.F., McWilliams, J.C., 2009. Correction and commentary for ocean forecasting in Terrain-following coordinates: Formulation and skill assessment of the regional ocean modeling system by Haidvogel, others. J. Comput. Phys. 227, 3595–3624. http://dx.doi.org/10.1016/j.jcp.2009.09.002, Computational Physics 228, 8985–9000.

Shriver, J.F., Arbic, B.K., Richman, J.G., Ray, R.D., Metzger, E.J., Wallcraft, A.J., Timko, P.G., 2012. An evaluation of the barotropic and internal tides in a high resolution global ocean circulation model. J. Geophys. Res. 117 (C10024), http://dx.doi.org/10.1029/2012JC008170.

Simmons, H.L., Alford, M.H., 2012. Simulating the long-range swell of internal waves generated by ocean storms. Oceanography 25, 30–41. http://dx.doi.org/10.5670/oceanog.2012.39.

Simmons, H.L., Hallberg, R.W., Arbic, B.K., 2004. Internal wave generation in a global baroclinic tide model. Deep-Sea Res. II 51, 3043–3068. http://dx.doi.org/10.1016/j.dsr2.2004.09.015.

Sinnett, G., Fedderson, F., Lucas, A.J., Pawlak, G., Terrill, E., 2018. Observations of nonlinear internal wave run-up to the surfzone. J. Phys. Oceanogr. 48, 531–554. http://dx.doi.org/10.1175/JPO-D-17-0210.1.

Skamarock, W.C., Klemp, J.B., Dudhia, J., Gill, D.O., Barker, D.M., Duda, M.G., Huang, X.-Y., Wang, W., Powers, J.G., 2008. A Description of the Advanced Research WRF Version 3. NCAR Tech. No. NCAR/TN-475+STR, http://dx.doi.org/10.5065/D68S4MVH.

Tuerena, R.E., Williams, R.G., Mahaffey, C., Vic, C., Green, J.A.M., Naveira-Garabato, A., Forryan, A., Sharples, J., 2019. Internal tides drive nutrient fluxes into the deep chlorophyll maximum over mid-ocean ridges. Glob. Biogeochem. Cycles 33, 995–1009. http://dx.doi.org/10.1029/2019GB006214.

van Haren, H., St. Laurent, L., Marshall, D., 2004. Small and mesoscale processes and their impact on the large scale: an introduction. Deep-Sea Res. II 51, 2883–2887. http://dx.doi.org/10.1016/j.dsr2.2004.09.010.

Wallcraft, A., Carroll, S.N., Kelly, K.A., Rushing, K.V., 2003. Hybrid Coordinate Ocean Model (HYCOM) Version 2.1. User's Guide. p. 76.

Wang, X., Chao, Y., Li, Z., Farrara, J., Dong, C., McWilliams, J.C., Shum, C.K., Wang, Y., Matsumoto, K., Rosenfield, L.K., Paduan, J.D., 2006. Tidal simulation using Regional Ocean Modeling System (ROMS). In: ESA Altimetry Meeting. p. 6.

Wang, J., Fu, L.-L., Qiu, B., Menemenlis, D., Farrar, J.T., Chao, Y., Thompson, A.F., Flexas, M.M., 2018. An observing system simulation experiment for the calibration and validation of the surface water ocean topography sea surface height measurement using in situ platforms. Atmos. Ocean. Technol. 35, 281–297. http://dx.doi.org/10.1175/JTECH-D-17-0076.1.

Waterhouse, A.F., MacKinnon, J.A., Nash, J.D., Alford, M.H., Kunze, E., Simmons, H.L., Polzin, K.L., St. Laurent, L.C., Sun, O.M., Pinkel, R., Talley, L.D., Whalen, C.B., Huussen, T.N., Carter, G.S., Fer, I., Waterman, S., Garabato, A.C.N., Sanford, T.B., Lee, C.M., 2014. Global patterns of diapycnal mixing from measurements of the turbulent dissipation rate. J. Phys. Oceanogr. 44, 1854–1872. http://dx.doi.org/10.1175/JPO-D-13-0104.1.

Zamudio, L., Hogan, P., Metzger, E.J., 2008. Summer generation of the Southern Gulf of California eddy train. J. Geophys. Res. 113 (C06020), http://dx.doi.org/10.1029/2007JC004467.

Zaron, E.D., 2019. Baroclinic tidal sea level from exact-repeat mission altimetry. J. Phys. Oceanogr. 49, 193–210. http://dx.doi.org/10.1175/JPO-D-18-0127.1.

Zaron, E.D., Egbert, G.D., 2014. Time-variable refraction of the internal tide at the Hawaiian ridge. J. Phys. Oceanogr. 44, 538–557. http://dx.doi.org/10.1175/JPO-D-12-0238.1.

Zaron, E.D., Elipot, S., 2021. An assessment of global ocean barotropic tide models using geodetic mission altimetry and surface drifters. J. Phys. Oceanogr. 51, 63–82. http://dx.doi.org/10.1175/JPO-D-20-0089.1.